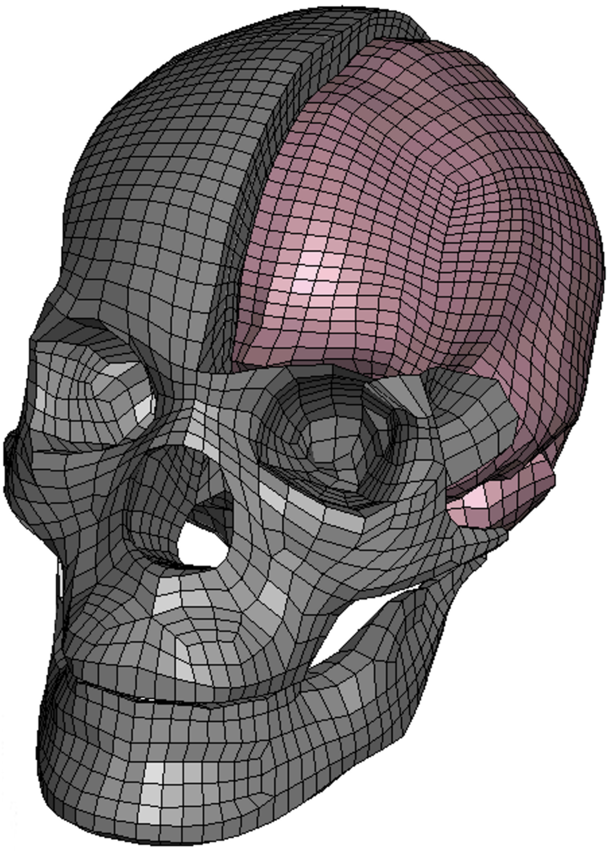

Material Modeling of the Human Skull and Brain

Bachelor Thesis in Mechanical Engineering and Biomedical Engineering

Amanda Hansen
Jacob Johansson-Näslund
Odinn Pálsson

DEPARTMENT OF MECHANICS AND MARITIME SCIENCES
CHALMERS UNIVERSITY OF TECHNOLOGY
Gothenburg, Sweden 2026
www.chalmers.se

Bachelor thesis in Mechanical Engineering

Material Modeling of the Human Skull and Brain

Amanda Hansen
Jacob Johansson-Näslund
Odinn Pálsson

Department of Mechanics and Maritime Sciences
Division of Vehicle Safety
Chalmers University of Technology
Gothenburg 2026

Material Modeling of the Human Skull and Brain
Amanda Hansen
Jacob Johansson-Näslund
Odinn Pálsson

Supervisor: Johan Iraeus and Jobin John
Examiner: Johan Davidsson, Mechanical Engineering
Bachelor thesis 2026
Department of Mechanics and Maritime Sciences
Chalmers University of Technology
SE-412 96 Gothenburg
Telephone +46 31 772 1000

Cover: Figure of Skull and Brain in LS-Prepost software.
Typeset in LaTeX
Gothenburg, Sweden 2026

Material Modeling of the Human Skull and Brain
Amanda Hansen, Jacob Johansson-Näslund, Odinn Pálsson
Department of Mechanics and Maritime Sciences
Chalmers University of Technology

Abstract

Head injuries are a leading cause of mortality and disability among adults. To understand and prevent these injuries, Finite Element (FE) models, such as VIVA+, are used to simulate and analyze injury mechanisms in the human body. Although the VIVA+ model exhibits high biofidelity in many aspects, the current material models for the skull and brain have been insufficient. The skull has previously been modeled with a constant stiffness with MAT_024 that fails to capture the strain rate dependent behavior of bone tissue. The brain has been modeled using general properties for adipose tissue (fat) without validation against physical tests. The purpose of this study was therefore to identify, evaluate, and implement improved material models for the skull and brain in VIVA+ to enable more accurate injury prediction.

The work was divided into two parallel parts. For the skull, the MAT_187 material model was implemented, enabling strain rate-dependent adjustment of stiffness during impact. This model was validated through simulations replicating the blunt impact experiments of Raymond et al. and the drop tests reported by Loyd et al. For the brain, hyperelastic parameters for an Ogden material model (MAT_077_O) were re-optimized for gray matter, white matter, and the cerebellum, based on previously published experimental data. The resulting brain material model was subsequently validated by comparing simulated relative brain motion with experimental measurements obtained from human cadaver studies conducted by Hardy et al.

The results demonstrate that the implementation of MAT_187 for the skull was highly effective. The model successfully captured the strain rate-dependent behavior without relying on predefined constants and provided highly accurate predictions of both acceleration and impact stiffness, particularly in the drop test scenarios. For the brain, the optimized material parameters showed good agreement with experimental data at the material level. However, validation of the complete head model revealed a systematic overestimation of brain displacement during impact.

In conclusion, MAT_187 constitutes a versatile and highly effective approach for simulating the dynamic response of the skull. For the brain however, the findings indicate that an advanced material model alone is insufficient to achieve accurate biofidelity. To improve predictive capability, the VIVA+ model likely requires the inclusion of additional anatomical structures, such as the meninges, which play a critical role in damping and constraining brain motion in vivo.
Keywords: Finite element method, Human body model, Head injury, Brain tissue, Cortical bone, Material model

Preface

This Bachelor's thesis, comprising 15 higher education credits, was conducted during the spring semester of 2026 by undergraduate students from the Mechanical Engineering program. The project was provided by and carried out at the Department of Mechanics and Maritime Sciences at Chalmers University of Technology.

The work presented in this thesis is part of a larger, ongoing research project at Chalmers dedicated to the development of an open-source Human Body Model (HBM) known as VIVA+.

This report is primarily aimed at readers with a foundational understanding of solid mechanics and finite element analysis (FEA).

Acknowledgements

We would like to express our sincere gratitude to our supervisors, Johan Iraeus and Jobin John, for their incredible support, guidance, and for always being available to help us throughout the entirety of this work.

We would also like to thank Stina Granholm and Anton Back for taking the time to help us understand their previous work regarding the MAT_024 material model. Finally, a special thanks to Victor S. Alvarez for sharing his files on the brain validation setup, which were of great assistance to our project

Amanda Hansen
Jacob Johansson-Näslund
Odinn Pálsson
Gothenburg, May 2026

Contents

1

Introduction

Head injuries represent one of the most significant causes of mortality and disabilities in the adult population [1]. The severity of head injuries spans from superficial cuts to critical damage involving the skull and brain tissue. Injuries to the skull are primarily fractures, ranging from linear cracks to more complex depressed fracture [2], which occur when impact forces exceed the bone's structural tolerance. While the skull acts as a crucial physical barrier that absorbs impact energy, its structural failure can directly compromise or expose the underlying tissue. Specifically, injuries affecting the brain are classified as Traumatic Brain Injury (TBI), a particularly severe subcategory that accounts for approximately 37% of all injury-related deaths in Europe [3]. To reduce these numbers, improved injury prevention is essential, which requires a deeper understanding of head biomechanics.

1.1 Evolution of Human Injury Risk Assessment

The pursuit of understanding and preventing injuries has evolved through several stages of biofidelity (how accurate the model is compared to a human). Initially, injuries were studied using clinical observations of volunteers, i.e from the military [4]. However, due to ethical and safety constraints, volunteers can only be subjected to low-severity impacts. To investigate injury mechanisms under higher loading conditions, researchers used Post-Mortem Human Subjects (PMHS), more commonly known as cadavers.

Although this is a sufficient substitute for living humans, it is ethically and logistically challenging. Thus, physical Anthropomorphic Test Devices (ATDs) were developed, commonly referred to as crash test dummies, which uses test data from the PMHS to be verified [5]. While useful, these dummies are mechanical simplifications and expensive. To solve this, numerical simulations of these dummies were made. Although these were more cost efficient they only simulated the dummy and not the actual human and thus, still mechanically simplified. Today, the focus has shifted back toward simulating the actual human anatomy. These models are refereed to as Human Body Models (HBMs), with several prominent examples including VIVA+, PIPER, SAFER, THUMS and GHBMC. These models utilize the Finite Element Method (FEM), which allows for a detailed representation of complex geometries and material properties by dividing the anatomy into a finite number of elements. By using FE-based HBMs, researchers and engineers can analyze internal stresses and strains in specific tissues, such as the brain and skull, providing a level of biofidelity that physical dummies cannot achieve.

1.2 VIVA+ Human Body Models

This project uses models from the VIVA+ HBM catalog which is a set of open source, finite element HBMs, containing female and male models in seated and standing positions [6]. These models were developed with the intention of addressing sex-specific differences in injury outcomes [7]. The VIVA+ models were developed primarily for studying skeletal injuries, therefore non-skeletal joints and organs were represented by simplified structures [7].

During the development of the models the seated female was used as a base model and other models such as the seated male were derivatives of the base model. The differences between the models are only their node coordinates and mass distribution allowing for more models to be created by altering the nodes coordinates and the mass distribution [7].

1.3 Problem

While VIVA+ HBMs have reached a relatively high levels of biofidelity in certain body regions, they are currently not considered complete. There is an ongoing need to implement more advanced material models that have been strictly verified and validated against physical experimental tests. In particular, the skull and brain represent areas where existing material models either lack verification and validation or the results are insufficient.

Material models within the simulation environment are defined in the LS-Dyna Manual (Volume II) [8], which provides definitions for approximately 300 different material models. These models establish constitutive equations and relationships between various physical variables, allowing for the mechanical response of biological tissue to be modeled.

In early versions of the VIVA+ models the skull was modeled using MAT_020 (Rigid), a formulation for entirely non-deformable materials. While further developments have introduced the use of MAT_024 (Piecewise Linear Plasticity), this model failed to capture the strain rate dependent behavior in the bone. For the brain, the most recent model version uses adipose tissue (fat) material properties in MAT_077_O (Ogden rubber model) as a surrogate to achieve realistic mass distribution. However, no brain-specific material properties have been implemented or verified, and no brain-specific validations have been performed.

1.4 Purpose

The purpose of this project is to identify and evaluate material models of the skull and brain in the VIVA+ head model. By calibrating material parameters against test data and validating the head model against real-world experiments, the goal is to improve biofidelity and enable more accurate prediction of head injury mechanisms.

1.5 Scope

To ensure a feasible study within the given time frame, the scope of this project is focused on the following key areas. First, although VIVA+ is a full-body model, the analysis is strictly limited to the biomechanical response of the skull and brain, i.e interactions with the cervical spine and the rest of the body are not analyzed. Furthermore, no modifications will be made to the underlying mesh; instead, the study evaluates the predictive accuracy of the current available version of VIVA+ (v2.0.1), using only updated material models. Additionally, the scope is restricted to the analysis of blunt impacts, as penetration mechanics and ballistic-specific trauma are not considered.

In terms of computational tools, the study is limited to the use of LS-Dyna as the sole finite element solver. No comparative analysis between different solvers will be conducted, as the project focuses on the performance of the VIVA+ model within its native environment.

2

Theory

The purpose of this chapter is to present the theoretical concepts such as the Finite Element Method, LS-Dyna, and the material properties for both the skull and brain. Furthermore, it introduces an overview of studies that have been used to validate the model.

2.1 Overview of the Finite Element Method (FEM)

The finite element method (FEM) is used to model and optimize structures in a variety of fields [9]. It is a numerical tool that can approximate physical behaviour such as deformation, limit loads and heat transfer. This is a powerful tool for complex structures when analytical equations are impossible to implement or experimental methods are too expensive.

The first step of FEM is to perform a discretization of the structure, dividing it into a finite number of elements [9]. This is the fundamental idea of FEM, hence the name. This generates a mesh consisting of finite elements that are connected at points called nodes. The finite elements can be represented as 1D (Line), 2D (Surface) and 3D (Volume). Common types of elements are triangles and quadrilaterals for the 2D domain and tetrahedra and hexahedra for the 3D domain.

When the meshing is complete, shape functions are assigned to each element to approximate the displacement field within their element. The shape functions serve as interpolation functions to relate the values at the nodes to within the element [9]. The shape functions are most commonly polynomials and their degree depends on the element type.

Each element in the mesh has a specific stiffness matrix (K^e) representing their stiffness in all degrees of freedom (DoF) at each node [9]. For example, a 2D triangular element has a 6×6 stiffness matrix because it possesses two degrees of freedom at each of its three nodes, corresponding to the x and y directions. The stiffness depends on the material and geometry of the element and is derived from elasticity. Each element also has a load vector (f^e) derived from elasticity [9]. The elasticity equation is one of the governing equations in FEM. It is a differential equation that can be used to derive the integrals that need to be solved for the stiffness matrix and load vector. These calculations are done for each element and the matrices and vectors are then assembled into one global stiffness matrix (K) and load vector (f) that can be used to solve the final system of equations.

For FEM to work certain boundary conditions need to be prescribed. There are two types of boundary conditions in FEM, essential and natural boundary conditions [9]. The essential boundary conditions (also known as Dirichlet) prescribe the known displacements of the structure. The natural boundary conditions (also known as Neumann) prescribe external forces or stresses on the structure and are the derivative of the essential boundary condition. These boundary conditions are incorporated in the global stiffness matrix and load vector, making them solvable.

When the global stiffness matrix and load vector are complete the system of equations becomes $Ka = f$ [9]. Where K is the stiffness matrix, a is the displacement vector and f is the load vector. The unknowns are usually in the displacement vector except if the displacement is prescribed in which case the unknown becomes the reaction force in the load vector. These equations can be solved using either explicit or implicit numerical methods. The implicit method calculates the equations for multiple iterations, achieving equilibrium in each timestep. This method is primarily used for slow and static problems. The explicit method calculates the next timestep directly from the systems current state, making it better for fast, non-linear events such as impact tests.

Finally the results are post-processed. The calculated displacements and forces can be used to evaluate internal variables such as stresses and strains in the structure [9].

2.1.1 LS-DYNA

LS-DYNA is a program for simulating and solving finite element problems and is popular in mechanics and dynamics-oriented industries [10]. The program's strengths lie in the simulation of complex transient and non-linear problems, where large deformations and irregular material behavior occur and events take place at high speeds or short time intervals.

To calculate the behavior of a dynamic system LS-DYNA solves the dynamic equilibrium equation, which for a single degree of freedom system can be formulated according to Equation 2.1 [11]. The equation describes the equilibrium between inertia, damping, internal and external forces acting on the system

$$m\ddot{u} + c\dot{u} + ku = p(t) \tag{2.1}$$

For multidimensional problems the equations become more complex and for non-linear dynamics, analytical solutions are generally not possible [11]. To solve such problems, LS-DYNA uses explicit time integration (central difference method [11]) in which the state of a system is calculated directly from the current state without the need for iterative equilibrium solutions [12]. This approach is commonly used in simulations of drop tests, vehicle crashes and also human body impacts, making it suitable for this project.

2.2 Material Properties of the Skull

A significant challenge in digital modeling is accurately representing the material of the human skull and brain. In the late 1960s and early 1970s, extensive experimental research was conducted by Wood [13, 14] to establish the fundamental mechanical properties of the human cortical bone of the cranium. Building upon this, Back et al. [15] implemented this into a FE model to further evaluate the results.

2.2.1 Mechanical Properties of Human Skull Bone

In Wood's doctoral dissertation, *Mechanical Properties of Human Cranial Bone in Tension* (1969) [13], and the subsequent publication, *Dynamic response of human cranial bone* (1971) [14], he investigated the tensile properties of compact cranial bone using specimens from the frontal, parietal, and temporal bones.

The specimens were machined into a specific geometry known as a 'dog bone' shape, see Figure 2.1. This design ensures a one dimensional flow of tensile stress within the test section.

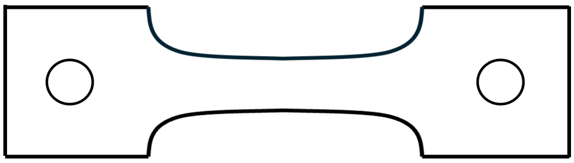

Figure 2.1. Specimen shape used in Wood's doctoral dissertation.

Wood's research established that the skull has strain rate dependent tissue properties, meaning it behaves differently depending on the speed of the impact. Beyond its rate dependent nature, several key mechanical and structural characteristics of the human skull were identified.

The cranial bone exhibits a brittle response, characterized by a low breaking strain and uneven fracture surfaces [14]. While the material appears linear at strains below 0.3%, the stress-strain relationship becomes increasingly non-linear as it approaches failure. Furthermore, the bone demonstrates strain softening behavior, meaning it becomes softer with strain [13].

Structurally, the skull is not a homogeneous solid. According to Wood it is a layered composite consisting of three parts: two outer layers of dense, compact bone known as the inner and outer tables, and a middle layer of porous, shock-absorbing bone called the diploë. This layered structure results in transversely isotropic behavior. This means the bone's mechanical properties are uniform when measured in any direction along the skull's surface [13].

2.2.2 Previous Analysis of Mechanical Properties of the Skull Bone

Building upon Wood's studies, Back et al. [15] investigated the sensitivity to age, sex and strain rate demonstrating the potential for such comprehensive material models to improve the predictive accuracy of human head simulations. This work highlights that these specific factors influence the skull's response and should be accounted for in high-fidelity simulations.

They created a regression model for all the data in Wood's doctoral dissertation and tried to implement this in a material model in LS-DYNA.

However, implementing these multi-faced properties (rate-dependency, non-linearity and biological variations) within a single FE-solver presents a technical challenge. Back et al. modeled the material of the cranial bone in the skull with MAT_024, which rely on a constant Young's modulus. Therefore, it will fail to capture the full complexity of the skull's dynamic behavior. Back et al. suggests further studies using MAT_187 allowing greater biofidelity in many ways, especially by accounting for strain rate dependency.

2.3 Anatomy of the Brain

Anatomically, the brain consists of three principal subdivisions: the cerebrum (the largest component); the cerebellum (often called the "little brain"), located beneath the posterior cerebrum; and the inferior brainstem [16]. See Figure 2.2 for illustration.

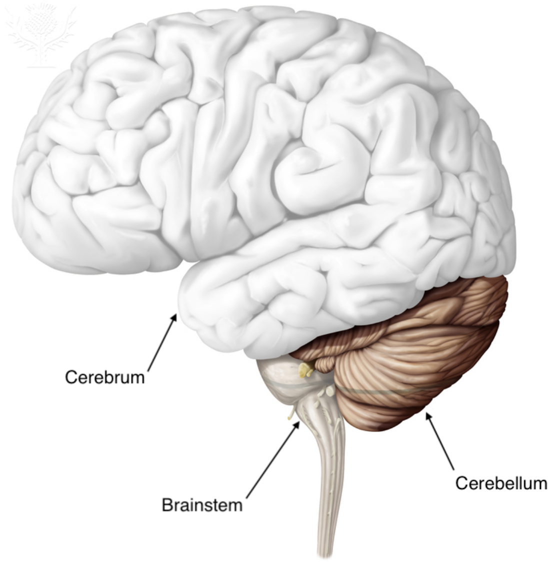

Figure 2.2. The main parts of the brain [17]

The brain is primarily composed of two distinct tissue types: gray matter and white matter [16]. Gray matter makes up the outer part of the brain and is predominantly composed of neuronal cell bodies (somas). Conversely, the white matter lies beneath the gray matter in the brain and consists primarily of axons [16]. The names reflect their contrasting appearances in scans of the brain, where the soma-rich gray matter appears distinctly darker than the white matter. Like the brain, the spinal cord is composed of these two tissue types. However, their arrangement is inverted, with the white matter forming the superficial layer and the gray matter at the core [16].

The superficial layer of the cerebrum, termed the cerebral cortex, is composed of gray matter, whereas the underlying deep tissue consists of white matter [16]. The cortex is folded, forming ridges and folds known as gyri and sulci, to maximize its functional surface area. As a result of this extensive folding, the cerebral cortex accounts for approximately half of the total brain mass [16].

The cerebellum is roughly the size of a clenched fist and structurally parallels the cerebrum. Like the cerebrum, it is organized into a superficial folded layer of gray matter and a deep core of white matter [16].

Serving as the junction between the cerebrum and the spinal cord is the brainstem. Its primary physiological role is to facilitate the transmission of neural signals between the brain and the rest of the body [16].

Between the brain and the skull are the meninges, which form a system of three protective membranes [16], see Figure 2.3. The outermost layer, the dura mater, lies in direct contact with the cranial bone. This robust membrane is composed of two distinct layers, which diverge in specific areas to accommodate the venous and arterial blood supply [16]. Deep to the dura mater lies the arachnoid mater, a thinner membrane characterized by its web-like connective tissue [16]. The third and innermost layer, the highly vascularized pia mater, tightly adheres to the surface of the brain, following its contours [16].

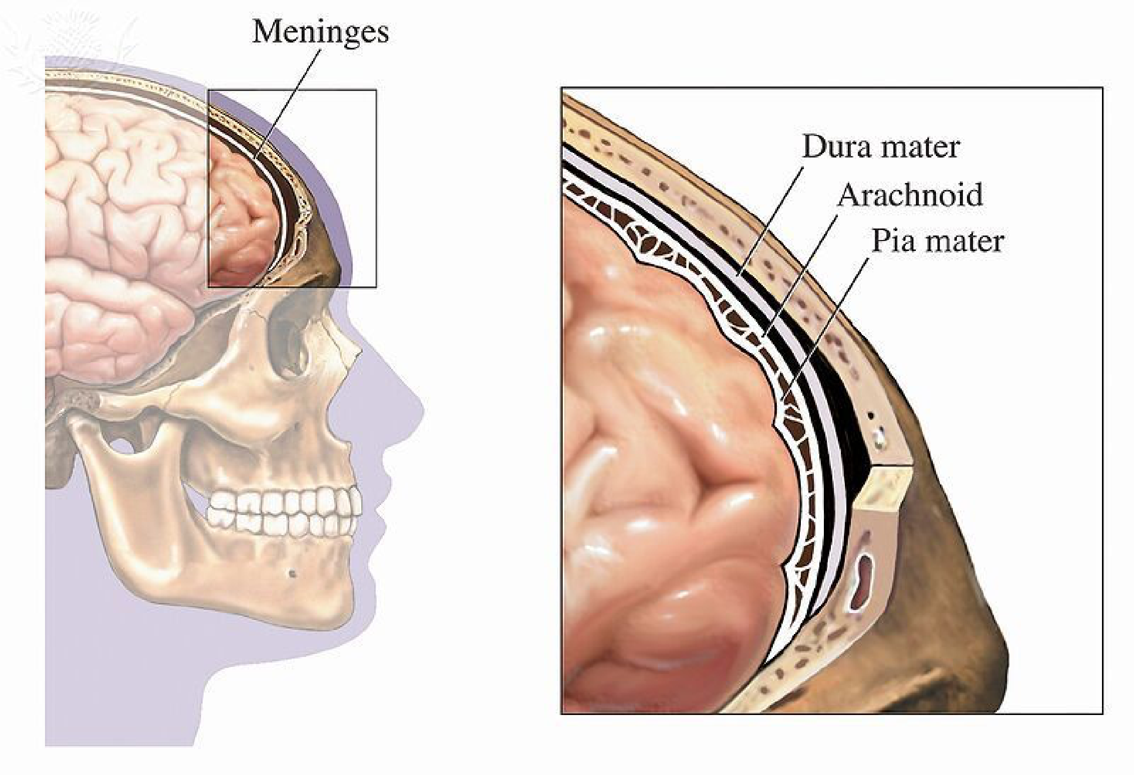

Figure 2.3. The layers of the meninges [18]

Between the arachnoid and pia mater lies the subarachnoid space, which contains cerebrospinal fluid (CSF) [16]. The CSF serves as a mechanical shock absorber for the central nervous system and circulates continuously to clear metabolic waste [16].

The major subdivisions of the brain are separated by dural reflections—inward folds of the dura mater that constrain the movement of neural tissue [19]. The largest of these is the falx cerebri, which lies between the two cerebral hemispheres [19]. Another notable reflection is the tentorium cerebelli, which horizontally separates the cerebrum and cerebellum [19]. Together, this network of membranes constrains the overall kinematics of the brain, thereby minimizing internal displacements and rotations [19].

2.4 Material Properties of the Brain

As mentioned above the brain consists of gray and white matter, the meninges and dural reflections as well as CSF. This section aims to describe the mechanical properties of these tissue types.

In a study by Badar et al. porcine brain tissue properties and responses under load are defined [20]. The researchers state that the porcine brain is strain-rate dependent, meaning that the brain gets stiffer for higher strain-rates. The researchers also found that the tissue is viscoelastic and has a non-linear stress-strain behaviour.

This means that the tissue's structural response is fundamentally time-dependent, simultaneously exhibiting both solid-like elasticity and fluid-like energy dissipation and its stiffness changes disproportionately as it is compressed. Finally, brain tissue is also modeled as a nearly incompressible material, meaning that it maintains a constant overall volume during deformation [20].

Because the brain consists primarily of white and gray matter, characterizing the distinctions between these two tissue types is of great importance. In a study conducted by Budday et al. the mechanical properties of white and gray matter from bovine brain was studied [21]. The researchers found that on average white matter was 39% stiffer than gray matter. Another finding by the researchers was that white matter is also more viscous and responds less rapidly to mechanical loading compared to gray matter.

Due to the limited availability of experimental data on human brain tissue, the studies discussed in this chapter rely on porcine and bovine brain tissue. Consequently, a critical assumption underlying this work is the biological and mechanical comparability between these animal models and human tissue—an assumption that ultimately requires further empirical verification.

2.5 Data for Skull Model Validation

The empirical basis for validating the skull's biomechanical response is primarily derived from two foundational studies: the blunt impact tests conducted by Raymond et al. (Section 2.5.1) and the drop tests by Loyd et al.(Section 2.5.2).

2.5.1 Raymond et al.'s Blunt Impact Tests

Raymond et al. (2009) subjected seven Post Mortem Human Subject (PMHS) heads to a total of fourteen blunt ballistic impacts [22], four female PHMS and three male. Utilizing an instrumented 38.1 mm rigid projectile, each specimen experienced two distinct impact conditions delivered to the bilateral temporo-parietal regions (illustrated in Figure 2.4): a lower-speed impact with a target velocity of 20 m/s on one side, and a higher-speed impact targeting 35 m/s on the other side.

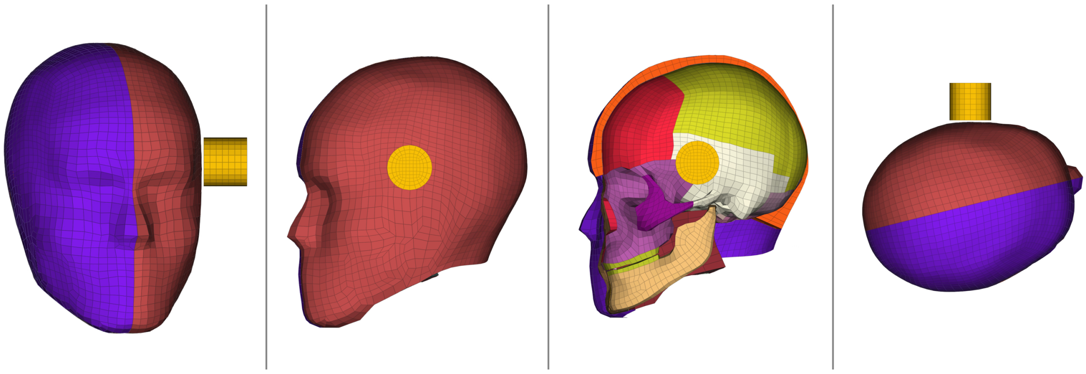

Figure 2.4. Impact location for Raymond's blunt impact tests.

Measurements of the impactor's acceleration were made and from these, several critical variables were analytically derived; impact force was calculated by applying Newton's Second Law to the projectile's known mass and measured acceleration. Furthermore, linear and rotational head accelerations were mathematically transformed to the head's center-of-gravity, principal and maximum shear strains were computed via specialized formulas based on the tri-axial gauge readings, and the energy-based Blunt Criterion (BC) was evaluated utilizing projectile kinematics alongside the local combined thickness of the subject's soft tissue and skull [22].

2.5.2 Loyd et al. Drop Tests

Loyd et al. [23, 24] investigated the impact response of the human head compared to various Anthropomorphic Test Devices (ATDs) by dropping specimens onto a rigid surface. The study utilized six male Post Mortem Human Subjects (PMHS) heads and seven different ATD heads. To ensure non-destructive testing and avoiding fractures, the heads were released from nominal target heights of approximately 15 cm and 30 cm; however, the exact measured drop height varied slightly for each individual test. Impacts were evaluated at five distinct location: the forehead, occiput, vertex, right parietal and left parietal, as illustrated in Figure 2.5.

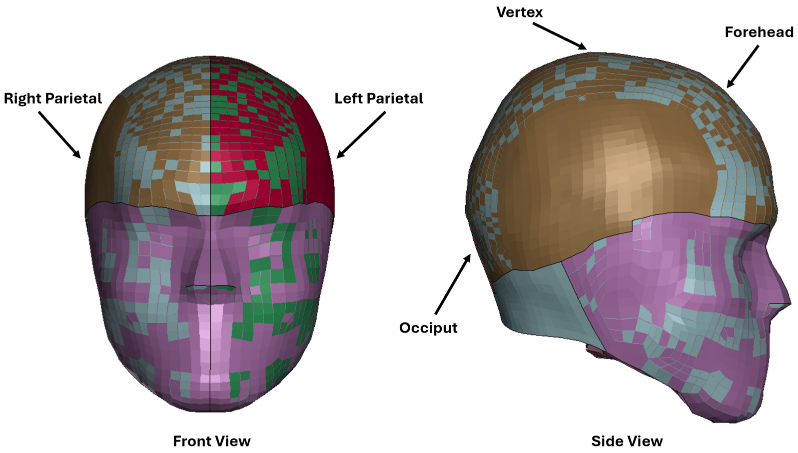

Figure 2.5. Impact location for Loyd et al. drop tests.

In this study the impact force was measured directly and subsequently used to determine acceleration through Newton's second law, where acceleration is defined as the ratio of force to mass. From the resulting acceleration-time history, the peak resultant acceleration and the Head Injury Criterion (HIC) [25] values were calculated. Additionally, the displacement during impact was obtained by double integrating the acceleration data. Furthermore, impact stiffness was determined by generating force-displacement curves, where a linear regression was applied from 50% of the peak displacement up to the point of peak force.

To ensure technical accuracy and minimize noise, all recorded data were filtered. The research employed the SAEj211b Class 1000 filter specification [26], which is the standard for head impact instrumentation

2.6 Data for Brain Model Validation

To address the absence of brain-specific material parameters in the VIVA+ model, the brain's mechanical properties were studied to obtain a reliable initial estimation for brain model simulations. The following data was used for identification of brain material model parameters and brain motion validation simulations.

2.6.1 Overview of Brain Material Modeling in Rycman et al.

In a 2024 study, Rycman et al. [27] sought to improve a contemporary FE head model with regard to brain material accuracy and skull-brain interface representation. The study was based on the GHBMC average stature male head model (version 6.0), which is an already well-developed model [28].

To improve the material representation in the head model, experimental data from porcine brain tissue was used to fit material parameters to an Ogden-based hyperviscoelastic model. The Ogden material model was chosen to account for key brain characteristics such as asymmetry between tension and compression, rate dependency and non-linearity.

The dataset from the porcine experiments was extensive, covering four different brain regions (gray matter, white matter, brainstem and cerebellum), three modes of loading (compression, tension and shear) and three different strain rates ($0.01s^{-1}$, $1s^{-1}$ and $50s^{-1}$) [29][30]. The data was digitized and laid the groundwork for the fitting of four different parameter sets, corresponding to the different brain regions.

The fitting followed a structured and detailed procedure. Two-term functions for hyperelastic strain energy and viscoelastic stress were simultaneously fitted to their respective portions of the stress-strain curves. The viscoelastic coefficients were fitted using all three modes of loading whereas the hyperelastic terms were only fitted with tension and compression, from which the shear response is then implicitly determined by the Ogden model. The fitting was done for the four regional datasets but only the lowest strain rate ($0.01s^{-1}$) curves for the hyperelastic function since a quasi-static formualtion was used.

The fit optimization aimed to minimize the difference between the experimental stress-strain responses and corresponding simulation responses from LS-DYNA which was integrated in a commercial optimization tool(LS-OPT). The resulting parameters from the optimization was used as a baseline for the present study and are presented in Table 2.1

Table 2.1. Material parameters from Rycman et al. [27]

Brain region	**Hyperelastic parameters**	**Viscoelastic parameters**	**General parameters**
Gray matter	$\mu_1 = 1.468$ MPa $\alpha_1 = 1.01 \times 10^{-3}$ $\mu_2 = -6.424$ Pa $\alpha_2 = -5.07$	$G_1 = 0.231$, $\beta_1 = 1\,s^{-1}$ $G_2 = 0.384$, $\beta_2 = 50\,s^{-1}$	$\nu = 0.49999$ $\rho = 1060\,\mathrm{kg\,m^{-3}}$
White matter	$\mu_1 = 1.687$ MPa $\alpha_1 = 1.16 \times 10^{-3}$ $\mu_2 = -0.555$ Pa $\alpha_2 = -8.3$	$G_1 = 0.213$, $\beta_1 = 1\,s^{-1}$ $G_2 = 0.483$, $\beta_2 = 50\,s^{-1}$	$\nu = 0.49999$ $\rho = 1060\,\mathrm{kg\,m^{-3}}$
Cerebellum	$\mu_1 = 1.600$ MPa $\alpha_1 = 1.1 \times 10^{-3}$ $\mu_2 = -0.716$ Pa $\alpha_2 = -5.12$	$G_1 = 0.259$, $\beta_1 = 1\,s^{-1}$ $G_2 = 0.382$, $\beta_2 = 50\,s^{-1}$	$\nu = 0.49999$ $\rho = 1060\,\mathrm{kg\,m^{-3}}$
Brainstem	$\mu_1 = 1.621$ MPa $\alpha_1 = 1.12 \times 10^{-3}$ $\mu_2 = -7.822$ Pa $\alpha_2 = -5.41$	$G_1 = 0.319$, $\beta_1 = 1\,s^{-1}$ $G_2 = 0.429$, $\beta_2 = 50\,s^{-1}$	$\nu = 0.49999$ $\rho = 1060\,\mathrm{kg\,m^{-3}}$

2.6.2 Hardy et al. Relative Motion of the Brain

Hardy et al. conducted a study which investigates the brain displacement and deformation in human cadaver models [31]. The study included eight head and neck specimens and a total of 35 impact tests were done. To better represent living conditions, the researchers used artificial cerebral spinal fluid to repressurize the specimens.

The method used to measure the displacements inside the brain was Neutral Density Targets (NDTs) [31]. Because these NDTs cause deformations and lacerations in the brain prior to the test Hardy et al. designed targets that gave an overall target density at or below 1.5 gm/ml. Each test utilized 14 NDTs, implanted in two clusters of seven and distributed either bilaterally or anteroposteriorly across the cranium, depending on the impact plane. Impacts in the coronal and horizontal planes had bilateral distribution, while impacts in the median plane had anteroposterior distribution, as seen in Figure 2.6. As the head was subjected to impact, a high-speed biplane x-ray system was used to image the clusters and follow their movement [31].

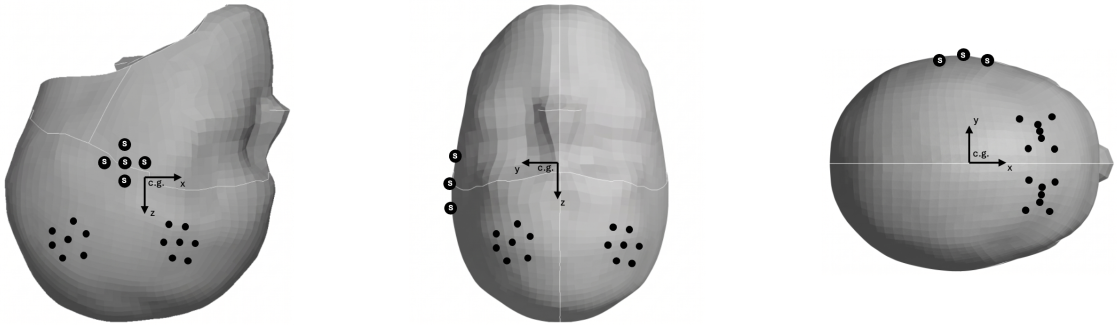

Figure 2.6. Positioning of NDT markers depending on impact plane, median (left), coronal (center) and horizontal (right)

The experimental setup consisted of a nine-accelerometer array, two cranial pressure transducers, a pneumatic piston and some of the specimens were fitted with an american football helmet to evaluate the effect of protective equipment [31]. The nine-accelerometer array and the two cranial pressure transducers were implanted in the specimens. One pressure transducer was placed at the site of impact to measure coup pressure (intracranial pressure at the site of impact) and the other was placed opposite the site of impact to measure contrecoup pressure (intracranial pressure opposite the site of impact). The accelerometer array measured the heads three-dimensional kinematics and the pressure transducers measured the transient pressure changes. To generate the impact the researchers used the pneumatic piston which could be controlled to hit the head at desired speeds [31].

By altering the impact positions the researchers obtained different responses from the brain [31]. The impacts were delivered in all three planes as well as offset and aligned with the CoG of the head to introduce rotations.

From the tests Hardy et al. concluded that the localized brain motions tend to follow figure-eight patterns and that the displacement of the brain lags the motion of the skull [31]. Hardy et al. also observed that peak average maximum principal and shear strains decreased as linear acceleration, coup pressure, and the rate of coup pressure increased. The helmet was found to reduce linear and angular accelerations but increased the strain.

3

Method

To address the research objectives, this work was divided into two parallel sub-projects: one investigating the skull, and the other investigating the brain. Both sub-projects followed a similar methodological approach. Initially, a literature review was conducted to establish the relevant material properties. Subsequently, the material models were verified, and ultimately the material model implementation were validated against data from physical experiments. This overall methodological workflow is illustrated in Figure 3.1. To isolate the effects of each component, the validation of the skull material model was performed independently of the updated material model of the brain, and vice versa. Thus, the validation of one sub-project did not rely on the updated brain models from the other.

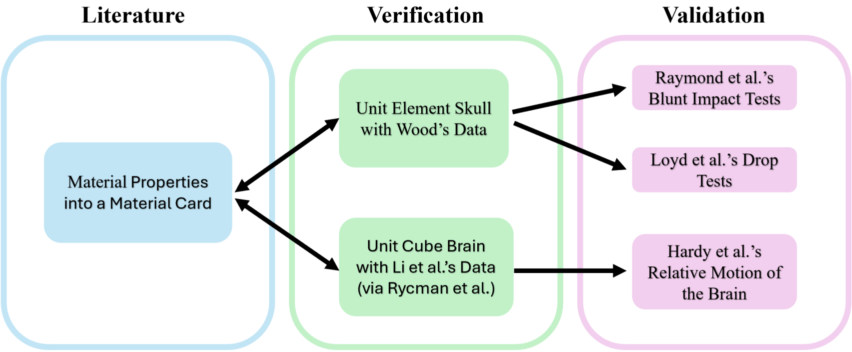

Figure 3.1. Flowchart illustrating the overall methodology used in this project

3.1 Implementation of the Skull's Material Model

To improve the predictive accuracy of the head model, the material representation of the skull's cranial bone was changed from the previously used MAT_024 (Piecewise Linear Plasticity) to the more advanced MAT_187, also known as MAT_SAMP-1 (Semi-Analytical Model for Polymers). This selection was motivated by the need to address the limitations identified in earlier research [15], where a constant Young's Modulus was insufficient to capture the skull's rate dependent behavior.

Unlike standard plasticity models, MAT_187 allows for a function-based linearity in the elastic region. This feature enables the definition of the modulus of elasticity as a function of strain rate, allowing the solver to adjust the material stiffness dynamically during the simulation. This is particularly critical for high-rate impact scenarios where the bone exhibits significant dynamic stiffening.

3.1.1 Material Model Input and Data Acquisition

The input parameters for the material model were derived from the experimental data provided by Wood [13, 14]. The model essentially needs three types of curves: Young's modulus as a function of strain rate, plastic Poisson's ratio as a function of plastic strain and the yield stress as a function of plastic strain.

Additionally, the material definition required two assumed parameters to ensure numerical stability. The density was set to $2 \cdot 10^{-6}$ kg/mm^3 and the decay constant was determined iteratively to $1 \cdot 10^{-5}$ ms^{-1}, as this value ensured numerical convergence even at low strain rates.

In this study, the plastic Poisson's ratio was maintained at a constant value of 0.43, based on the radial contraction measurements of compact cranial bone reported by Wood [13].

The yield stress curves were derived following the methodology described in the previous study using MAT_024 [15]. In that work, a Bayesian regression model was used to generate stress-strain curves based on experimental data from Wood [13]. To maintain the comparability of the statistical distributions established in that study, the resulting yield stress curves were implemented directly into the MAT_187 card without further modification. These curves were organized into a table and used as is, allowing the model to represent the non-linear transition from elastic deformation to failure based on the previously validated data for different strain rates.

The predictive model for Young's modulus was similarly adapted from the previous study. Since the original regression model by Back et al. required extensive sample-specific data, such as anatomical part and bone type, it was simplified to minimize the number of dependent variables, see Equation 3.1. This was done by simplifying the regression model that depends solely on strain rate, age and sex.

$$\begin{aligned}\text{Youngsmodulus}_i = \beta_0 + \beta_1 \cdot \log(\text{strainrate}_i) + \beta_2 \cdot \text{Age}_i \\ + \beta_3 \cdot \text{Sex[M]}_i\end{aligned} \tag{3.1}$$

In the thesis by Back et al. [15], material cards were developed for both a "base" model (representing a 50-year-old) and an "aged" model (representing an 80-year-old). The present study, however, exclusively utilizes the "base" material card.

3.1.2 Material Model Verification

To verify the material implementation, simulations were performed on unit elements, which were modeled in 2D using shell elements. This approach allows for a direct comparison with the tensile tests conducted by Wood, as the dogbone-shaped specimen (see section 2.2.1) used in those physical experiments were designed to ensure a state of one dimensional tensile stress within the test section.

The simulations were conducted to obtain stress as a function of strain across various strain rates. The resulting stress-strain curves were then compared with regression curves that the previous study [15] conducted using Wood's data [13]. This comparison was made to ensure that the current model accurately captures the rate-dependent behavior of the human cranial bone in a manner consistent with previous validated findings.

3.2 Head Impact Validation of the Skull's Material Model

For validation of this material model implementation, two studies were simulated using LS-Dyna. First, blunt impact tests to the temporo-parietal region to be able to directly compare the results to previous work with MAT_024 [15], and then drop tests performed at five different impact locations to further expand the validations.

3.2.1 Simulation of Blunt Impact tests to the Temporo-Parietal Region

To simulate Raymond et al.'s. blunt impact tests, a setup identical to the one described by Back et al. was utilized. They impacted the head with a rigid cylindrical impactor with a density corresponding to aluminum (2.7×10^{-6} kg/mm^3). The impact was directed at the temporo-parietal region, specifically 25 mm anterior to the external acoustic meatus and 35 mm superior to the Frankfurt plane, as illustrated in Figure 2.4 in Section 2.5.1.

For the base configuration of the current study, the 50th percentile male and female head models were employed. These base models were subsequently scaled according to Equation 3.2 (where the constant Head model mass is 4.416 kg) to more accurately replicate the size of the experimental specimens. The specific mass and corresponding scaling factor for each individual specimen are presented in Table 3.1. The only difference between this study and the methodology used by Back et al. is the implementation of the new material card with MAT_187. Finally, the necessary output variables from the simulations (such as displacement, time, force, and strain) were acquired using the post-processing tool Dynasaur [32].

$$\text{Scaling Factor} = \sqrt[3]{\frac{\text{PMHS Mass}}{\text{Head model mass}}} \tag{3.2}$$

Table 3.1. Mass and scaling factor for each specimen.

Specimen	Sex	Mass [kg]	Scaling Factor [-]
2426	M	3.26	0.90351
2427	M	2.98	0.87713
2904	M	4.30	0.99087
2908	F	3.48	0.96941
2939	F	3.28	0.95947
2965	F	3.42	0.96380
2978	F	3.10	0.93275

3.2.2 Simulation of Drop Tests at Five Different Impact Locations

The drop tests performed by Loyd et al. [23] were simulated by impacting the head model against a rigid floor. The floor was modeled as a 200 × 200 mm rigid shell with a density corresponding to aluminum (2.7×10^{-6} kg/mm^3). To replicate the experimental impact conditions, the head model was spatially transformed and oriented to strike the floor at the correct anatomical locations (the specific impact location are illustrated in Figure 2.5 in Section 2.5.2).

Furthermore, the material card, from the unit elements, was implemented and assigned to all parts of the skull identified as cortical bone. For each respective test, the impact velocity of the head was calculated based on the experimental drop height using Equation 3.3 where v is the initial impact velocity, g is the acceleration due to gravity, and h is the drop height. This calculated initial velocity was applied to all components of the head model prior to impact. To prevent any initial penetrations between the head and the rigid plate at the start of the simulation, a small initial gap was introduced. To analyze the simulation results, the primary data extracted was the contact force between the head and the rigid floor. To account for the initial gap and facilitate the comparison of the generated graphs, the output data was cropped to the relevant time frame, defined as the period during which the contact force remained above 100 N. This allowed for the calculation of all relevant impact variables using the same methodology as Loyd (see section 2.5.2). In addition, kinematic data, such as acceleration, were extracted from the center of gravity node to provide a basis for further comparison. This node represents the average displacement, velocity, and acceleration of all nodes located on the inside of the skull.

$$v = \sqrt{2gh} \tag{3.3}$$

All extracted data were filtered using an SAE J211b Class 1000 low-pass filter to ensure consistency with the experimental data processing. The calculated initial impact velocities for each test are presented in Table A.1-A.6 in Appendix A.

All simulations were initially conducted using a base head model, which represents an average sized 50-year-old male. In addition to the base variant, the tests were also performed using scaled models. The scaled models utilized the same material definitions as the base model, but the head geometries were scaled to correspond to the size of each specific subject. The scaling factor was determined using Equation 3.2 where the constant Head model mass is 4.416 kg. The individual PMHS masses and their corresponding calculated scaling factors are given in Table 3.2.

Table 3.2. Mass and scaling factor for each specimen.

Specimen	**Mass** $[kg]$	**Scaling Factor** [-]
A01M	3.16	0.89444
A02M	3.27	0.90470
A04M	3.21	0.89914
A05M	3.08	0.88683
A06M	3.41	0.91743
A07M	3.45	0.92101

3.3 Material Model Implementation for Brain Tissue

Since the current VIVA+ brain model lacks detailed material representation and testing, there was need to implement material models with suitable parameters for different substructures and to verify the implementation. This section describes the material parameter identification process, re-optimization methods and verification simulations that were performed.

3.3.1 Baseline Material Model Selection

As stated in the introduction of this report, the current VIVA+ brain model uses an Ogden rubber material model (MAT_077_O) where only the density is brain-specific to achieve accurate mass representation. To establish a baseline for the present study, brain-specific material parameters from Rycman et al. [27] were selected. These parameters had been fitted against extensive datasets and subsequent head model validations showed high levels of biofidelity. A summary of the material modeling approach can be found in section 2.6.1 as well as the selected baseline parameters (Table 2.1).

3.3.2 Verification of Brain Material Model and Parameter Implementation

To ensure that the baseline materials would behave as expected, verification simulations using simplified unit cubes were performed. The purpose of these simulations was to isolate the material response and compare the results with the stress-strain curves reported by Rycman et al. [27].

Three separate unit cube models were created to represent tension, compression and shear loading. Each cube consisted of a single solid element and the loading modes were implemented by prescribing nodal motion to the top surface, and applying suitable boundary constraints to prevent rigid body motion.

Three versions of these setups were created, where the baseline material parameters for gray matter, white matter and cerebellum were implemented. These were then simulated for the three different strain rates ($0.01s^{-1}$, $1s^{-1}$, and $50s^{-1}$) and the resulting stress-strain curves were extracted. No simulations for the brainstem material were performed since no stress-strain curves were available [27]. To allow for direct comparison, the simulated stress-strain curves reported [27] were digitized.

When comparing the results, notable differences were observed in the stress responses. For all materials, strain rates and modes of loading, the stress was lower compared to what was reported by Rycman et al. [27] and this was especially true at higher strains.

3.3.3 Re-Optimization of Brain Material Model Parameters

Because of the observed differences from the verification process, a re-optimization of the material parameters was performed in order to establish a more reliable basis for the continued study. The re-optimization was based on the same experimental data was as used in Rycman et al. [27](originally from Li et al [29]). This data was extracted by digitizing the experimental curves from plots in Rycman et al. [27]. Since no stress-strain curves were available for the brainstem [27], no optimization of its parameters were performed.

For this project, only the hyper-elastic parameters in the Ogden function were re-optimized. To do this, a two-term Ogden stress function was used (Equation 3.4), where the coefficients were fitted to data from the lowest strain rate ($0.01, s^{-1}$). The λ in Equation 3.4 represents the stretch ratio which is the deformed length divided by the original length. The experimental strain data for tension and compression, therefore had to be converted before the optimization procedure.

$$\sigma = \mu_1 \left(\lambda^{\alpha_1} - \lambda^{-0.5\alpha_1}\right) + \mu_2 \left(\lambda^{\alpha_2} - \lambda^{-0.5\alpha_2}\right) \tag{3.4}$$

The optimization of the parameter fit was performed by minimizing the sum of squared errors (SSE, Equation 3.5) between the experimental stress data and the stresses calculated from the Ogden function.

$$SSE = \sum_{i=1}^{n} \left(\sigma_{\mathrm{exp},i} - \sigma_{\mathrm{model},i}\right)^2 \tag{3.5}$$

This optimization was performed using the integrated solver in Microsoft Excel with the non-linear GRG solving method. The material parameters for gray matter, white matter and cerebellum were optimized. The coefficient of determination (R^2) was calculated for each fit in order to evaluate it's quality. This was done for the fitted stress-stretch ratio response which combined the tension and compression datasets.

3.3.4 Verification of Optimized Material Model

The re-optimized hyperelastic parameters were implemented together with the baseline viscoelastic parameters in order to evaluate the complete material model behaviour. The evalutaion was done by performing the unit cubes simulations with the new material models. The resulting stress-strain responses were then compared to the experimental data.

3.4 Validation of brain model

To validate that the simulated results are similar to the experimental results the optimized and verified material parameters were used in the complete VIVA+ head-model. The brainstem which was not optimized due to missing data was implemented with the parameters from Rycman et al. as seen in Table 2.1 [27].

Since the VIVA+ head model is symmetrical, the material parameters were the same for both sides. On each side there are six parts, twelve in total, that represent the brain. See Table 3.3 for materials used.

Table 3.3. Materials used in the brain

VIVA+ Brain Part	Material Used
HE-Brain	Brainstem (Not optimized)
HE-Brain-Cerebrum	Gray Matter
HE-Brain-Cerebrum-CSF	Head-CSF
HE-Brain-Cerebellum	Cerebellum
HE-Brain-Cerebellum-CSF	Head-CSF
HE-Brain-Corpus-Callosum	White Matter

The head-models motion was then prescribed using the measured velocities and accelerations from Hardy et al. as input load curves for LS-Dyna using the `DEFINE_CURVE` function [31]. The acceleration from Hardy et al. was reported in g:s but was integrated to the velocity and converted to units of mm/ms as this is the standard velocity unit used in this model. The curves were assigned to a rigid body at the heads Center of Gravity (CoG) using the `BOUNDARY_PRESCRIBED_MOTION_RIGID_LOCAL` keyword. Using `CONSTRAINED_RIGID_BODIES` the head was constrained to follow the motion of the CoG.

As described in the theory chapter, Hardy et al. used Neutral Density Targets (NDTs) to measure the relative displacement inside the brain and listed the positions of the NDTs for each test [31]. This was used to position `DISCRETE_SPHERE`

`_VOLUMES` in the same places in the VIVA+ model using `ELEMENT_DISCRETE_SPHERE_VOLUME`. To capture the interaction between the brain and the NDTs an `ALE_COUPLING_NODAL_PENALTY` formulation was used to constrain the NDT elements inside the brain mesh.

Because Hardy et al. describes the relative motion, a local coordinate system was implemented in the CoG using `DEFINE_COORDINATE_NODES`. It is however, not clear from the researchers whether a local or a global coordinate system was used. This study used a local coordinate system for all configurations and later reran the configurations with a global coordinate system for comparison. The local coordinate system was then used to measure the relative displacement in the simulations [31]. The `DATABASE_HISTORY_NODE_LOCAL_ID` was used to record the displacement in each NDT.

After running the simulations for the tests the resulting relative displacements were compared to the ones reported by Hardy et al. and the C380-T4 test was also compared to the one reported by Rycman et al. [27, 31].

4

Results

This chapter presents all results obtained in this study.

4.1 Implementation of the Skull's Material Model

The result from implementing the MAT_187 material model is presented here.

4.1.1 Material Model Input and Data Acquisition

The yield stress as a function of plastic strain from Back et al. [15] work is shown in Figure 4.1.

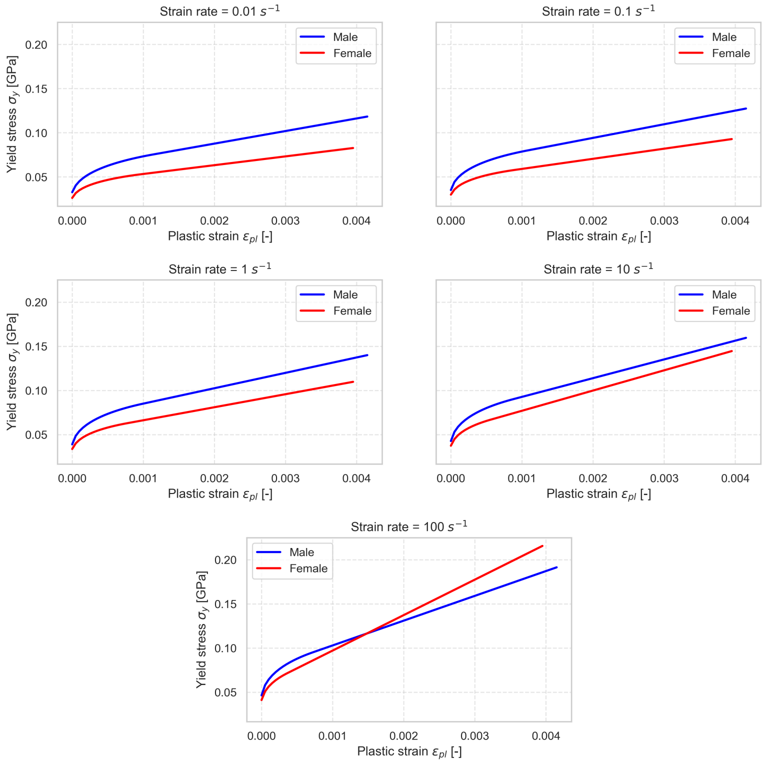

Figure 4.1. Yield stress as a function of plastic strain. Blue line is for the male model, red line is for female model.

The predictive model for Young's modulus as a function of strain rate could be substituted with Equation 3.1 in Section 3.1.1, with beta coefficients as shown in Table 4.1, the regressions error is also presented here that shows unexplained variance in the data. This function is shown in Figure 4.2 for the age of 50 years.

Table 4.1. Resulting β-coefficients for the regression model.

Coefficient	**Value**
β_0	16.389
β_1	1.573
β_2	-0.029
β_3	1.335
$Error$	1.197

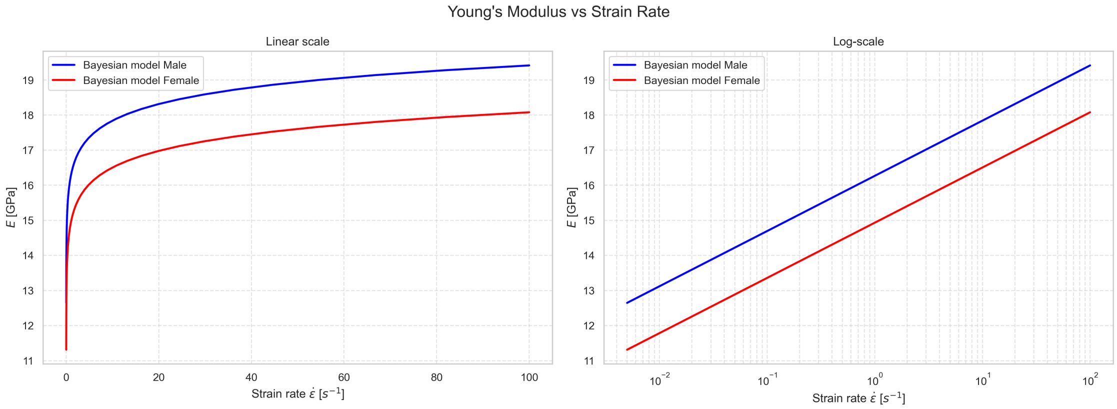

Figure 4.2. Young's Modulus as a function of strain rate. Blue line is for the male model, red line is for female model.

4.1.2 Material Model verification

The unit element's response with MAT_187 in tension is shown in Figure 4.3, for the male model, and Figure 4.4, for the female model. The response is compared to the regression model from Back et al. [15].

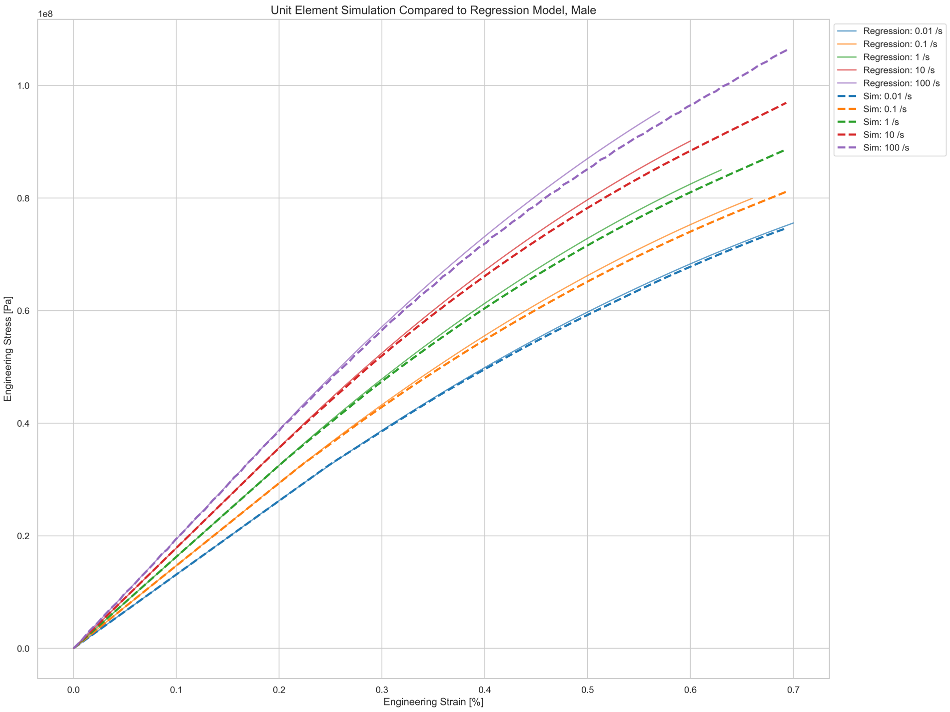

Figure 4.3. Stress as a function of strain from tensile test on a unit element at different strain rates. Male material model. Solid lines are the regression model, dashed lines are unit cubes response in simulation.

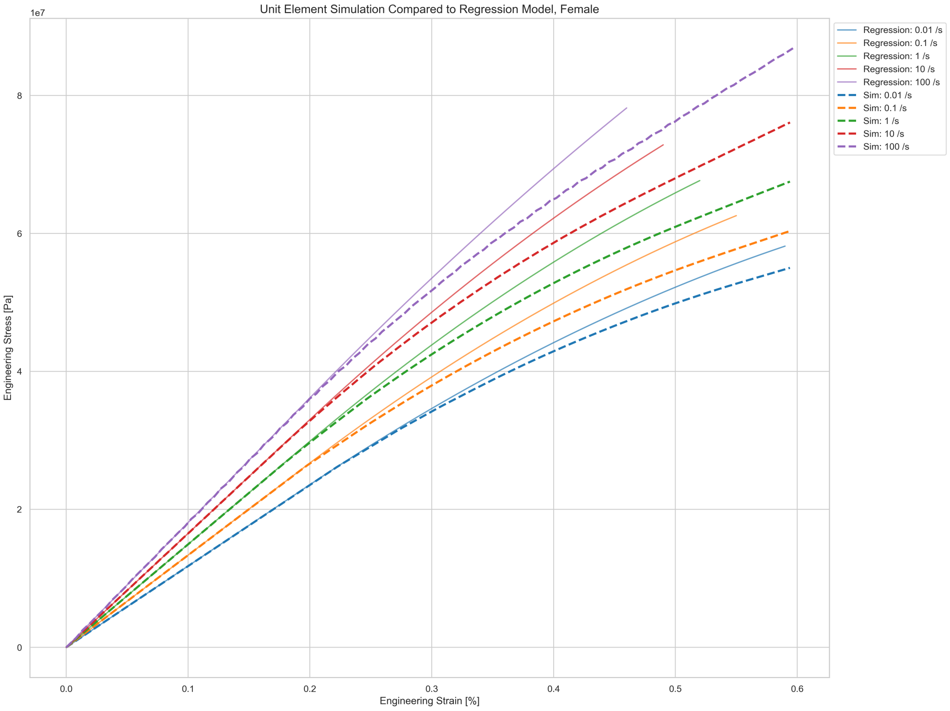

Figure 4.4. Stress as a function of strain from tensile test on a unit element at different strain rates. Female material model. Solid lines are the regression model, dashed lines are unit cubes response in simulation

4.2 Head Impact Validation of the Skull's Material Model

The results from the validation on the head model with the implementation of MAT_187 is presented below, both for Raymond et al.'s blunt impact tests and Loyd et al.'s drop tests.

4.2.1 Simulation of Blunt Impact tests to the Temporo-Parietal Region

Figure 4.5 presents the contact force as a function of deformation in the skull. Mat_187 is compared to MAT_024 from Back et al. work and the experimental results from Raymond et al.'s blunt impact tests for each specimen.

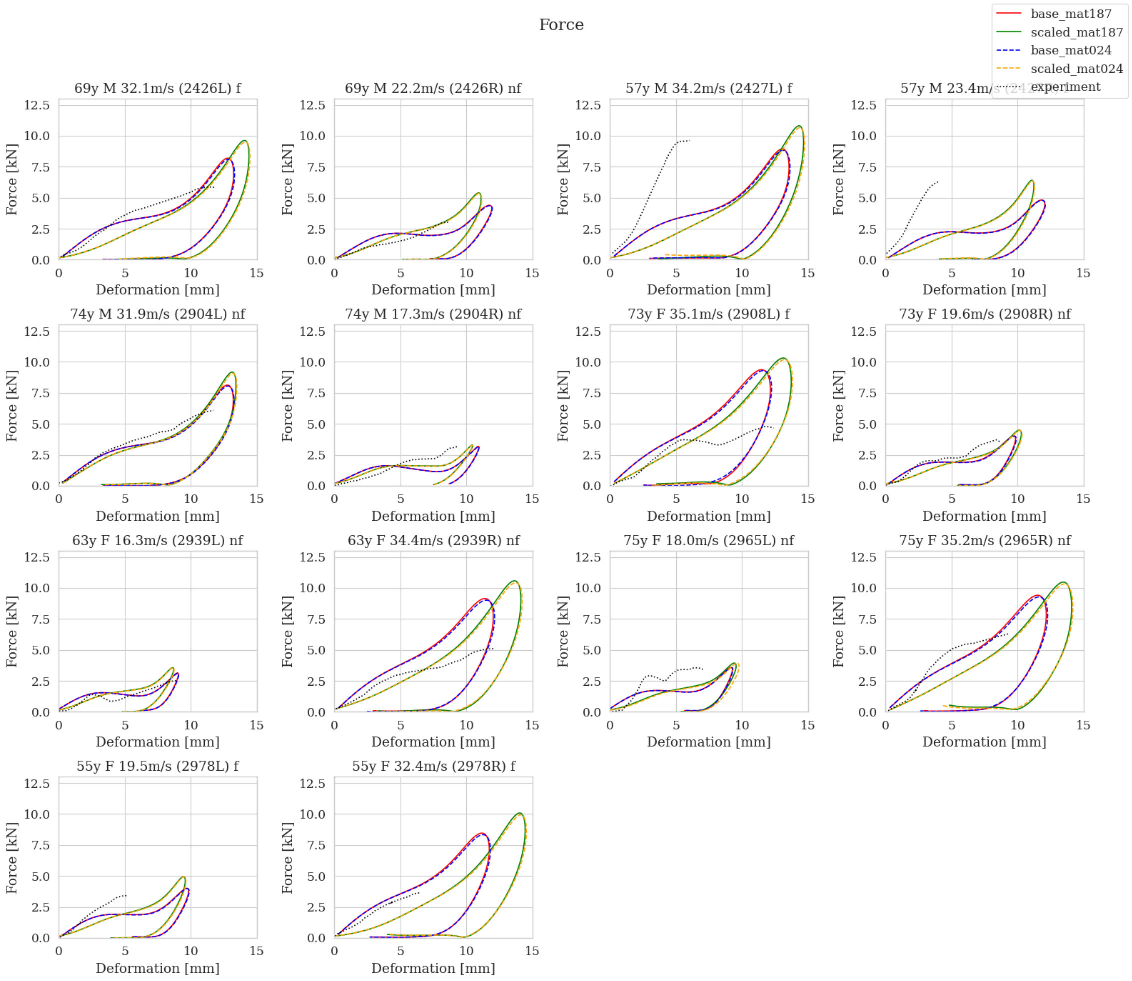

Figure 4.5. Force as a function of deformation, solid lines for MAT_187 and dashed lines for MAT_024, experimental lines are dotted.

4.2.2 Simulation of Drop Tests at Five Different Impact Locations

From the drop tests conducted by Loyd et al. [23], several different results could be compiled. However, this thesis focuses primarily on the acceleration and impact stiffness. As described i Section 3.2.2, the acceleration and displacement were extracted from the simulations using two distinct methods. First the exact values for each metric were extracted directly from the center of gravity node, which represent the average kinematic response of the inside of the skull. Second, estimated values were calculated solely based on the contact force. Figure 4.6 illustrates the relationship between these various quantities for the forehead drop test of specimen A01M from a drop height of approximately 15 cm. The individual acceleration-time histories for each specimen are presented in Appendix B, Figures B.1 - B.12.

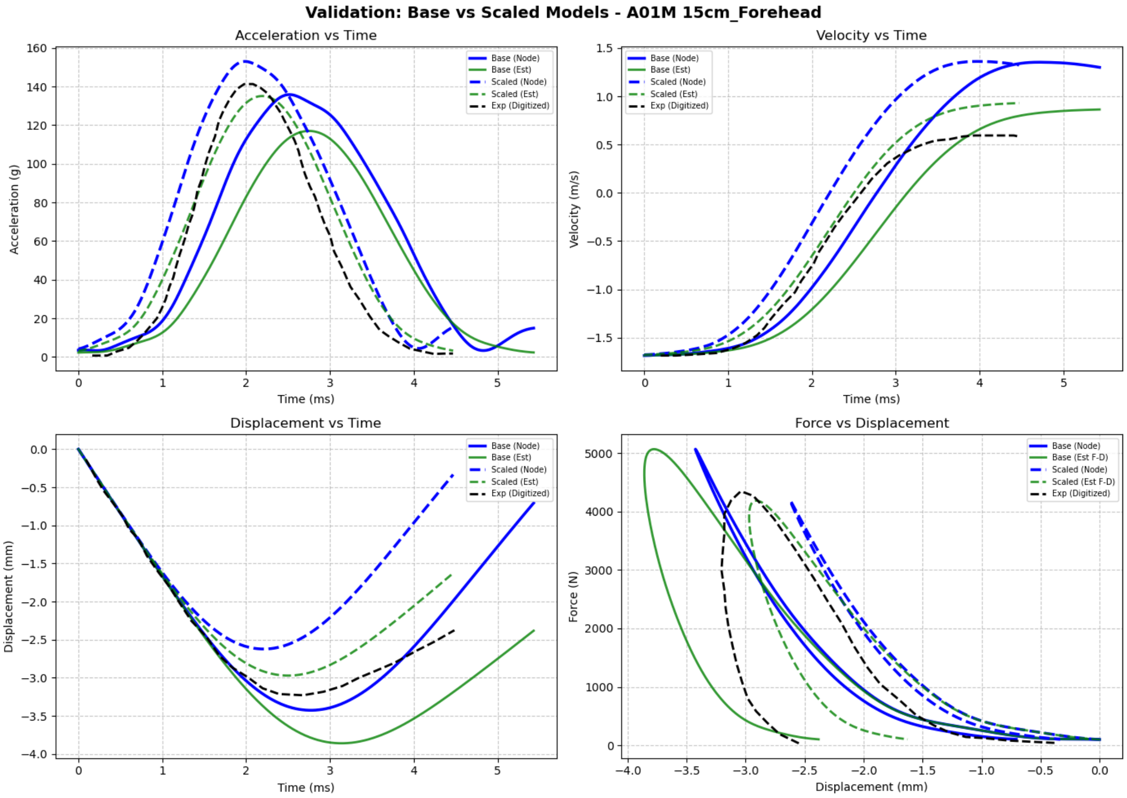

Figure 4.6. Plots of acceleration, displacement, velocity as a function of time and a plot of force as a function of displacement for Specimen A01M on the forehead from 15 cm. Black dashed line are the experimental data, other dashed lines represent the scaled model and solid lines represent the base model.

All of these values are summarized in the bar charts in Figure 4.7 for the base model and Figure 4.8 for the scaled model. In these figures the red bars represents the experimental data, the blue bars indicates the values extracted directly from the the nodes, and the green bars denotes the estimated values for the respective impact locations. Furthermore, all data for the right and left parietal impacts have been combined into a single 'parietal' category, as the VIVA+ HBM is completely symmetrical.

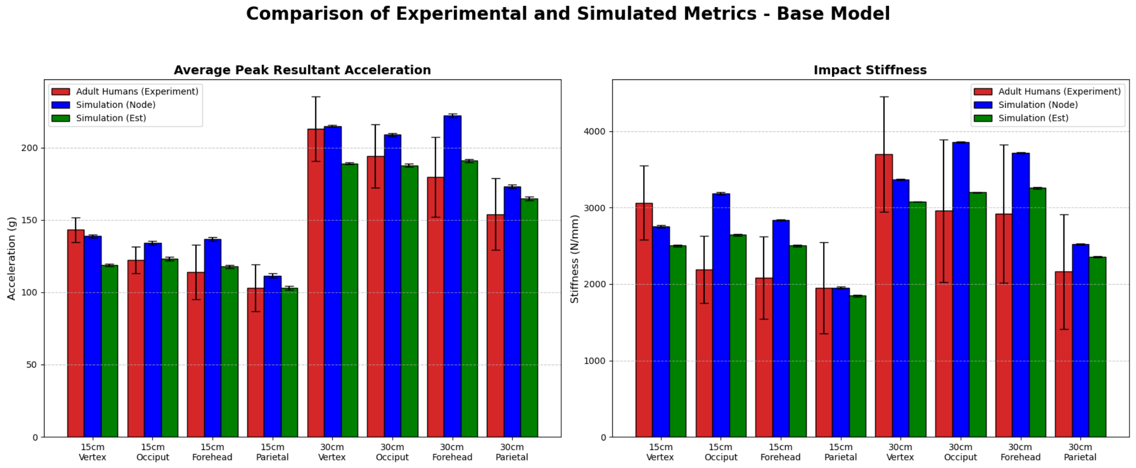

Figure 4.7. Bar chart illustrating the average peak resultant to the left and average impact stiffness to the right for each impact location for the base model.

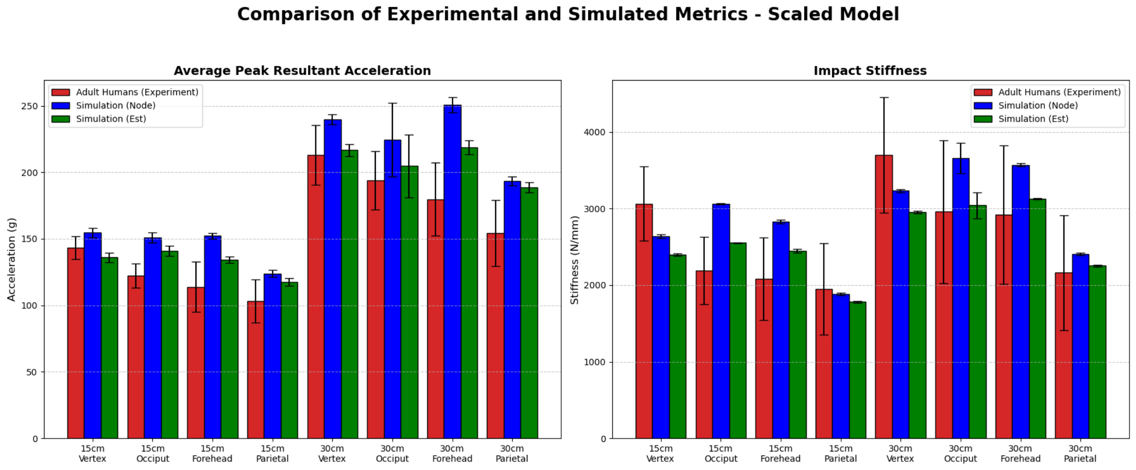

Figure 4.8. Bar chart illustrating the average peak resultant to the left and average impact stiffness to the right for each impact location for the scaled model.

To quantify the differences observed in the bar charts, the percentage deviation between simulation results and the experimental data was calculated for each configuration. A summary of these relative errors, covering both base and scaled models across all impact locations, is presented in Table 4.2.

Table 4.2. Deviation from experimental data for Base and Scaled models (%)

Impact Location	**Accel (Node)**	**Accel (Est)**	**Stiff (Node)**	**Stiff (Est)**
Base Model				
Vertex 15 cm	-3.0%	-17.0%	-10.1%	-18.3%
Occiput 15 cm	9.6%	0.8%	45.3%	20.8%
Forehead 15 cm	20.1%	3.4%	36.1%	20.1%
Parietal 15 cm	8.0%	-0.0%	0.0%	-5.3%
Vertex 30 cm	1.0%	-11.2%	-8.9%	-16.8%
Occiput 30 cm	7.6%	-3.2%	30.4%	8.1%
Forehead 30 cm	23.6%	6.3%	27.4%	11.7%
Parietal 30 cm	12.4%	6.9%	16.6%	8.9%
Mean Abs. Error (Base)	*10.7%*	*6.1%*	*21.9%*	*13.8%*
Scaled Model				
Vertex 15 cm	8.1%	-4.9%	-13.9%	-21.8%
Occiput 15 cm	23.5%	15.3%	39.7%	16.5%
Forehead 15 cm	33.7%	17.8%	35.7%	17.4%
Parietal 15 cm	20.0%	13.9%	-3.4%	-8.8%
Vertex 30 cm	12.6%	1.7%	-12.6%	-20.1%
Occiput 30 cm	15.7%	5.5%	23.7%	2.9%
Forehead 30 cm	39.4%	21.7%	22.4%	7.2%
Parietal 30 cm	25.6%	22.4%	11.2%	4.3%
Mean Abs. Error (Scaled)	*22.3%*	*12.9%*	*20.3%*	*12.4%*

4.3 Material Implementation for Brain Tissue

In this study, a number of methods were performed to identify, calibrate and verify material models and parameters for different regions in the brain. The results from these methods are presented in this section.

4.3.1 Verification of Baseline Material Parameters

For the verification of the baseline parameters, the simulated stress-strain responses curves was notably different to the curves presented by Rycman et al [27]. In Figure 4.9-4.11, direct comparisons between simulated constitutive responses in this study and the corresponding responses from [27] are presented. These figures show that the differences in the stress responses were found in all modes of loading and for all strain rates and increased with strain. Similar results were found for cerebellum and white matter (see Appendix C).

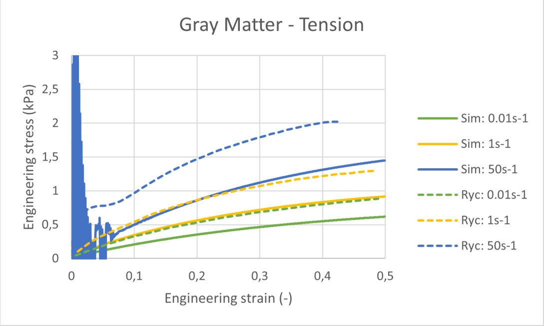

Figure 4.9. Simulated material responses using baseline parameters vs corresponding responses reported in Rycman et al. [27] for gray matter in tension.

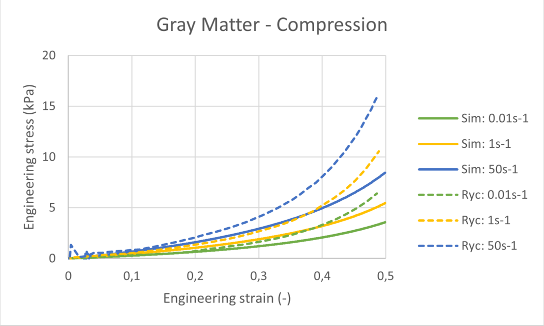

Figure 4.10. Simualted material responses using baseline parameters vs correspinding responses reported in Rycman et al. [27] for gray matter in compression.

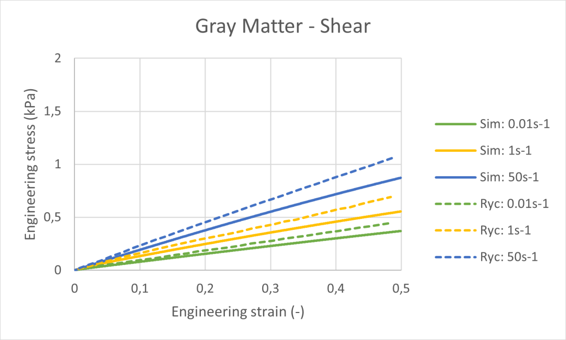

Figure 4.11. Simualted material responses using baseline parameters vs correspinding responses reported in Rycman et al. [27] for gray matter in shear.

4.3.2 Re-Optimization of Material Parameters

A two-term Ogden function was used to optimize the fit of the hyperelastic paramters against experimental data and the resulting parameters for the different materials are presented in Table 4.3. The quality of the fits were evaluated using the coefficient of determination (R^2). The R^2-value was calculated for the stress-stretch curves for the three materials and are also presented in Table 4.3.

Table 4.3. Optimized hyperelastic material parameters and R^2-measure of fit quality.

Material	**Optimized Parameters (Hyperelastic)**	R^2
Gray matter	$\mu_1 = 1.623$ MPa, $\alpha_1 = 1.12 \times 10^{-3}$ $\mu_2 = -4.06 \times 10^{-5}$ MPa, $\alpha_2 = -5.11$	0.99
White matter	$\mu_1 = 1.687$ MPa, $\alpha_1 = 1.16 \times 10^{-3}$ $\mu_2 = -5.3 \times 10^{-6}$ MPa, $\alpha_2 = -8.3$	0.98
Cerebellum	$\mu_1 = 1.796$ MPa, $\alpha_1 = 1.12 \times 10^{-3}$ $\mu_2 = -5.43 \times 10^{-5}$ MPa, $\alpha_2 = -5.25$	0.98

4.3.3 Optimized Material Model Verification Against Experimental Data

The verification simulations for the optimized material models showed overall good alignment with the experimental stress-strain data. The fitting was only done for the lowest strain-rate ($0.01s^{-1}$ and simulated stress-strain curves, generally matched better for the lower strain-rates. The material with the highest R^2-value from the optimization was gray matter and this corresponds well to the simulation results as seen in Figure 4.12-4.14.

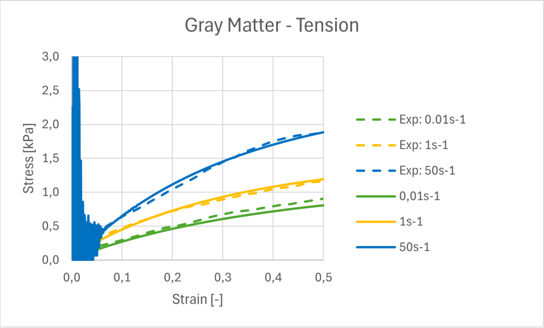

Figure 4.12. Optimized material model response vs experimental response for gray matter in tension.

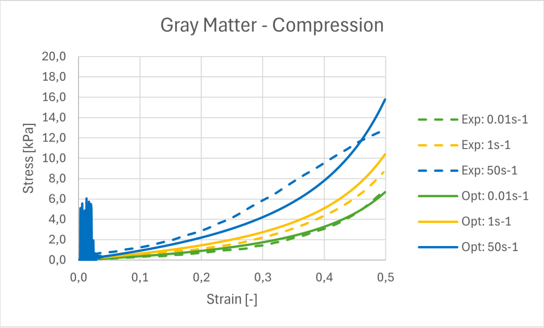

Figure 4.13. Optimized material model response vs experimental response for gray matter in compression.

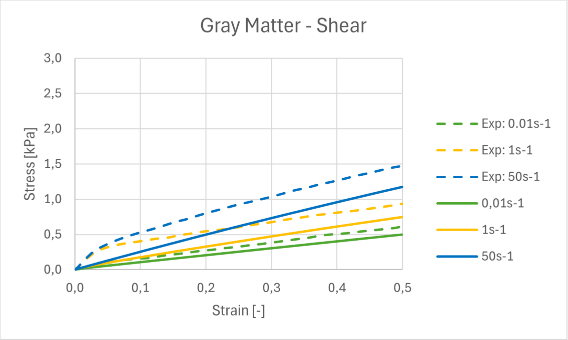

Figure 4.14. Optimized material model response vs experimental response for gray matter in shear.

4.4 Brain Motion Validation

This section presents the results from the simulations compared to the experimental results presented by Hardy et al. [31].

Figure 4.15 shows the simulated relative displacement compared to the experimental displacements presented by Hardy et al. in NDT 4 and NDT 11, X and Z direction [31]. This test had an offset impact in the median plane to the temporal region. In the experiment the specimen was not wearing a helmet.

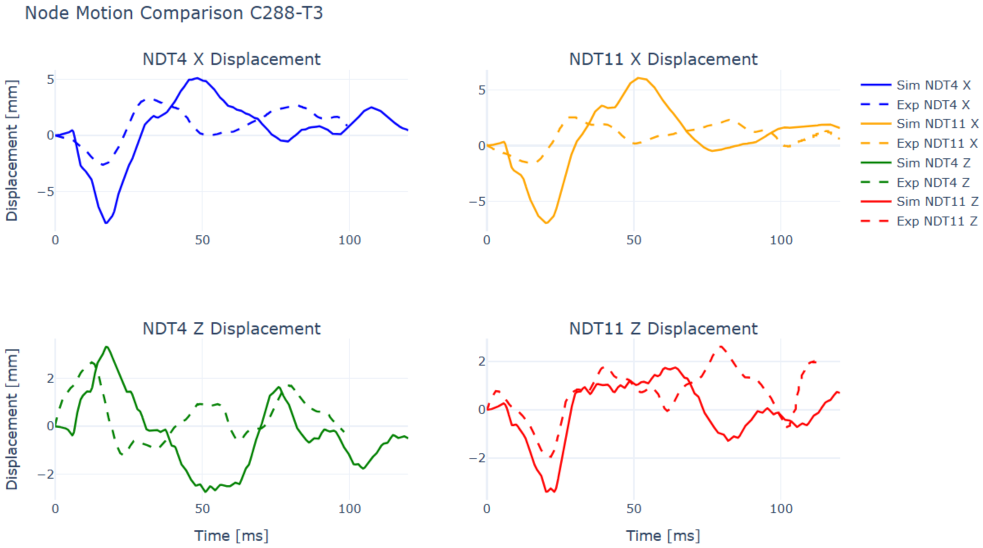

Figure 4.15. Simulated relative displacement (solid line) compared to Hardy et al. experimental relative displacement (dashed line) for specimen and test C288-T3

Figure 4.16 shows the simulated relative displacement compared to the experimental displacements presented by Hardy et al. in NDT 4 and NDT 11, Y and Z direction [31]. This test had an offset impact in the coronal plane to the temporal region. In the experiment the specimen was wearing a helmet.

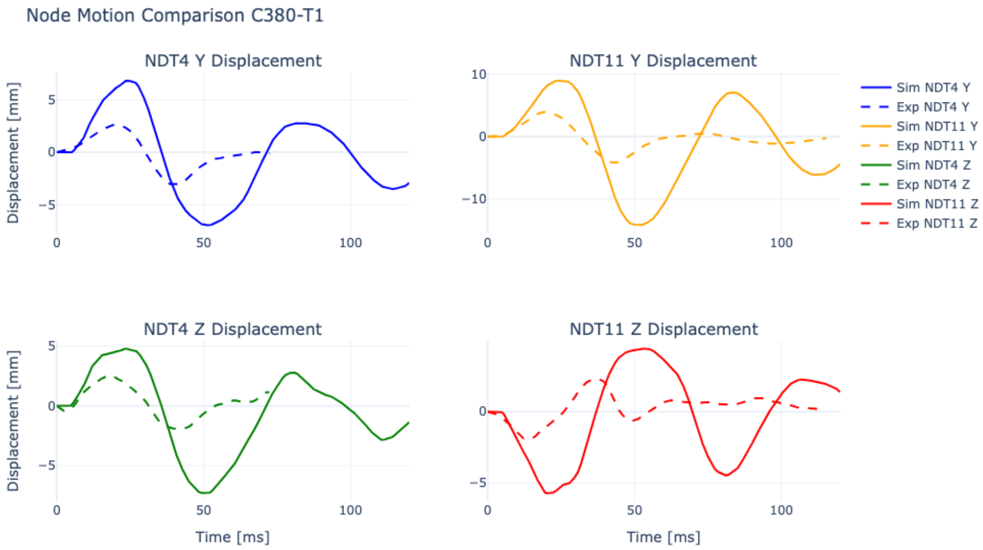

Figure 4.16. Simulated relative displacement (solid line) compared to Hardy et al. experimental relative displacement (dashed line) for specimen and test C380-T1

Figure 4.17 shows the simulated relative displacement compared to the experimental displacements presented by Hardy et al. in NDT 4 and NDT 11, X and Y direction [31]. This test had an offset impact in the horizontal plane to the parietal region. In the experiment the specimen was wearing a helmet.

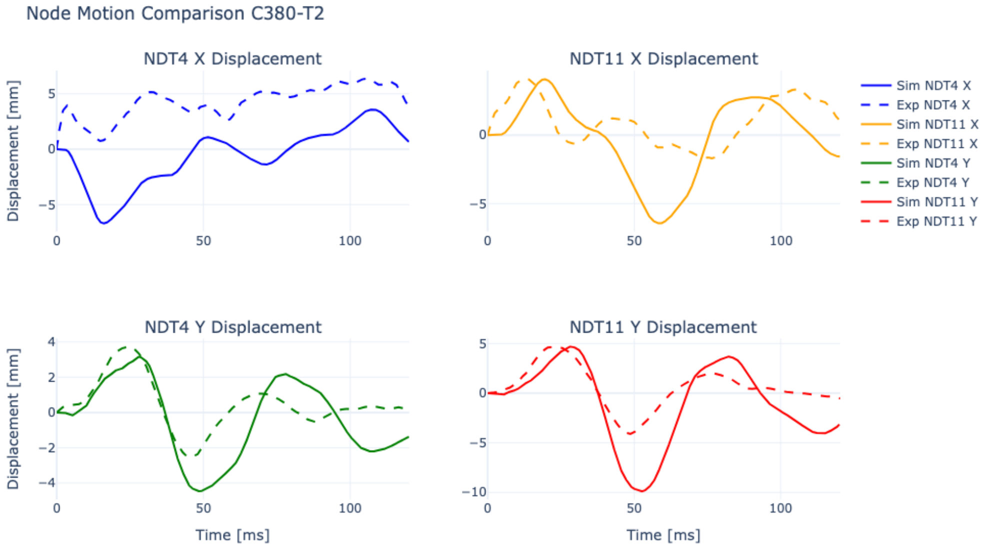

Figure 4.17. Simulated relative displacement (solid line) compared to Hardy et al. experimental relative displacement (dashed line) for specimen and test C380-T2

4.4.1 Comparison Between Local and Global Prescribed Motion

The difference between the local and global coordinate system implementation is shown in Figure 4.18 and Figure 4.19.

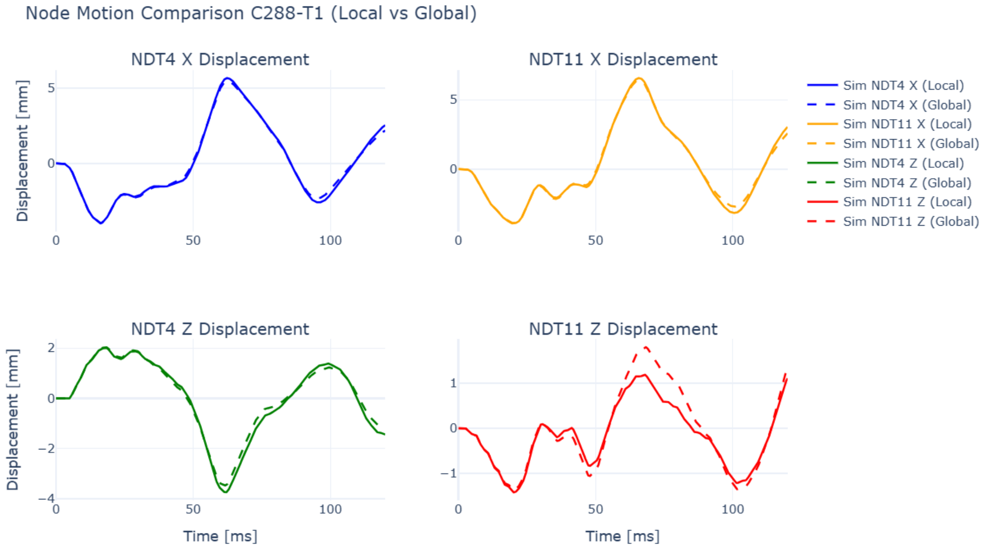

Figure 4.18. Comparison between local coordinates (solid) and global coordinates (dashed) for C288-T1.

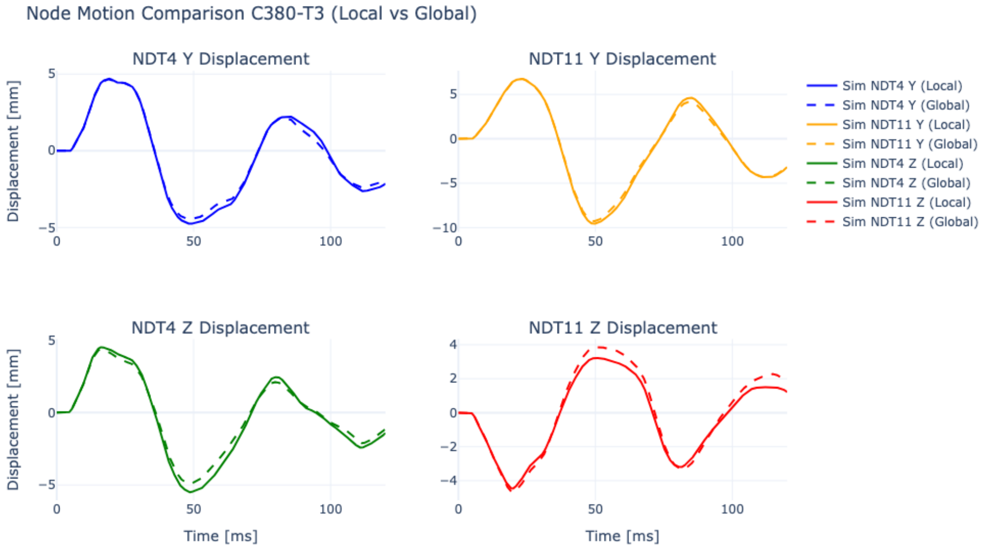

Figure 4.19. Comparison between local coordinates (solid) and global coordinates (dashed) for C380-T3.

4.4.2 Comparison to Results from Rycman et al.

The simulated relative displacement from the new material parameters were compared to simulations done with the material parameters from Rycman et al. [27]. See Figure 4.20 for comparison.

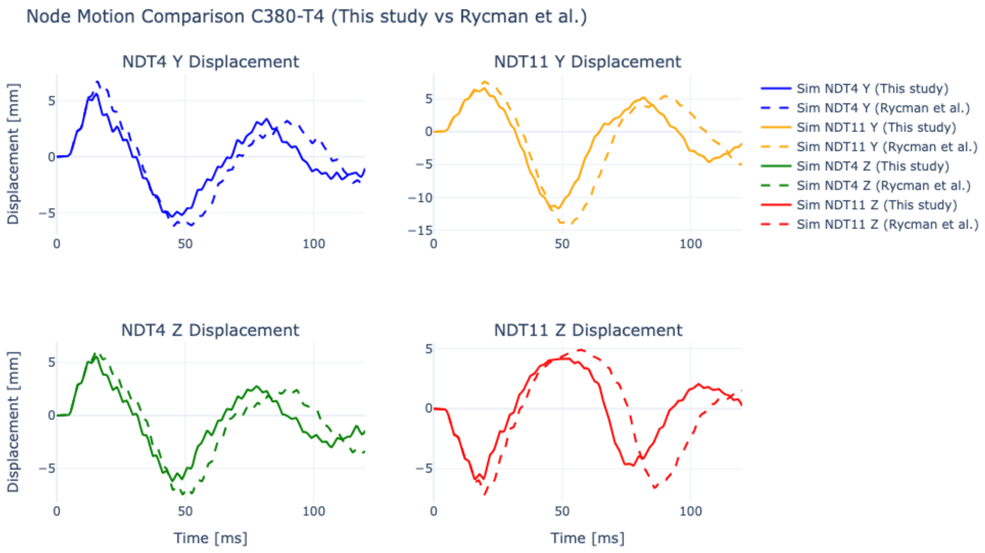

Figure 4.20. Simulated relative displacement (solid line) compared to Rycman et al. simulated relative displacement (dashed line) for specimen and test C380-T4

5

Discussion and Conclusion

The purpose of this final chapter is to discuss the results obtained from the computational simulations. The findings are evaluated against the validation studies. Furthermore, the limitations of the project are addressed followed by the main conclusions of the thesis and suggestions for future work.

5.1 Discussion on the Skull's Material Model

The verification process over the skull's unit elements demonstrated that the male material card closely matched the regression-model based stress-strain curves developed by Back et al. [15] from Wood's experimental data. The female material card also showed a strong correlation, although its accuracy was slightly lower than that of the male model. It can be seen that Young's modulus as a function of strain rate is highly accurate for both sexes. The simulated stress-strain curves are nearly identical to the regression models up to 0.2% strain, an initial region which according to Wood [13] is solely dependent on the Young's modulus.

However, beyond this initial point, the functions defining yield stress as a function of plastic strain governs the subsequent behavior of the curves. These relations could benefit from further finetuning. This adjustment is needed to a minor degree for the male model, but to a greater extent for the female model. Specifically, the simulated curves exhibits a slightly more pronounced curvature than the regression models predict, particularly at higher strain rates.

Furthermore, when examining the validations against the blunt impact tests conducted by Raymond et al. [22], it is evident that the MAT_187 material model yields nearly identical results to those obtained with MAT_024 in the previous work by Back et al. [15]. Unlike MAT_024, MAT_187 does not require a prior assumption regarding the applied strain rate on the skull in order to define the corresponding Young's modulus. Instead, MAT_187 inherently establishes this continuous relationship, providing an appropriate Young's modulus for any strain rate between $0.01s^{-1}$ and $100s^{-1}$. This continuous strain rate dependency creates a much more versatile model that can be utilized across various impact scenarios without the need to presume a specific, constant Young's modulus. Since the exact same relationship between yield stress and plastic strain was applied in both material models, obtaining comparable results is both reasonable and expected.

The second part of the validation focused on the drop tests conducted by Loyd et al. Overall, the simulation acceleration curves demonstrated a strong general resemblance to the experimental data. Generally, the acceleration data extracted from the center of gravity node yielded higher values than the estimated accelerations. Regarding the mean absolute deviation error, the most accurate overall configuration was the base model with estimated values, which presented a deviation to acceleration of only 6.1%. This outcome was anticipated, as it is highly plausible that the estimated values should serve as a better representation of the physical experiments. This expectation is reasonable since the estimation approach directly mirrors the methodology used to calculate and derive the accelerations during the actual physical tests.

When comparing the base and scaled models, the primary difference observed was that the scaled impact time was slightly shorter, resulting in a narrower and sharper peak in the acceleration curve. The scaled model demonstrated a slightly lower accuracy. This discrepancy can likely be attributed to the simplification of the scaling process; the head model was scaled proportionally in all directions rather than directly adjusting the specific scalp thickness to accurately represent each specimen.

Furthermore, when evaluating the impact stiffness, the results show that it is generally best approximated by utilizing the estimated values derived from either the base or scaled model. The base estimated values gives a mean deviation of 13.8% and the scaled estimate gives 12.4%. It is reasonable to expect the estimated values to perform better in this regard as well. As seen in the force-displacement plot (Figure 4.6), the estimated curves exhibit a much smoother profile that closely resembles the experimental data. Because impact stiffness is calculated by taking the slope between peek displacement and 50% of the peak displacement, any 'spikes' in the curve can severely distort the slope and lead to highly deviated values.

5.1.1 Conclusion on the Skull's Material Model

In conclusion the verification of the MAT_187 material model offers a versatile and highly effective approach for simulating the cranial bone response. By inherently capturing continuous strain rate dependencies for Young's modulus for strain rates ranging from $0.01s^{-1}$ to $100s^{-1}$, MAT_187 eliminates the need for predefined, constant strain rate assumptions. While the initial elastic response perfectly matches experimental data, the plastic yielding behavior (particularly for the female model) exhibits slightly pronounced curvature and would benefit from further fine tuning.

Additionally, validations against dynamic drop tests highlight the critical importance of both geometric scaling and appropriate data extraction methodologies. The base model, when evaluated using estimated acceleration and displacement values, yielded exceptionally accurate results, providing a highly reliable representation of both the acceleration and the overall impact stiffness.

5.2 Discussion on the Brain Material

A comparison of the simulated NDT motion against the Hardy et al. experimental data reveals a considerable overestimation of displacement in the model [31]. One possible reason is that the material is too soft as this would lead to greater motion of the NDTs. The eigenfrequencies of the simulations also indicate a material that is too soft. Since the eigenfrequency is proportional to the stiffness k and the mass m as in Equation 5.1. Provided that the mass is the same, a lower eigenfrequency means that the stiffness is too low.

$$f \propto \sqrt{\frac{k}{m}} \tag{5.1}$$

The VIVA+ model lacks a dedicated representation of the meninges layers and dural reflections, which could be another reason for the high deformations. These structures act as a constraint and dampener to the brains movements. Since the meninges and dural reflections were present in the Hardy et al. experiment but not in the VIVA+ model, the observed difference in deformations might be due to the missing anatomical structures in the mesh [31].

To collect acceleration data in the experiments, Hardy et al. used an array of accelerometers [31]. The researchers noted that the array had relative motion to the head that lead to noise in the measurement. A CFC 180-Hz filter was used for mitigation, this may however, filter some of the actual motion of the brain. This also means that the load curves that were digitized from Hardy et al. do not represent the actual velocities and accelerations of the head [31].

The simulations with the new material parameters were compared to the same configurations with parameters from Rycman et al. [27]. The results were very similar, showing the same general motion with the VIVA+ having slightly lower amplitude peaks and higher eigenfrequency. This indicates that the material parameters from this study are slighly stiffer but the difference is minimal. However, Rycman et al. report a considerably lower relative displacement from their simulations that were ran on the GHBMC [27]. This is likely due to the inclusion of the meninges and falx cerebri in the GHBMC which constrains the relative displacement of the NDTs in addition to the stiffness of the material.

Since there was some ambiguity in Hardy et al. [31] whether the reported acceleration data was with regard to global or local coordinate systems, simulations with both global and local prescribed motion were performed. When comparing the results of these simulations, the initial motions were practically identical, which is to be expected as the local and global coordinate system are aligned initially. Later in the simulations, small difference were observed but deemed not to be significant. Therefore, the local coordinate system was used for all simulations for consistency.

All material parameters for the Ogden-based materials were fitted against the experimental data originally reported by Li et al [29]. This data was gathered from porcine brain tissue and the study was primarily intended for pediatric purposes and thus used specimens from relatively young pigs [29]. In contrast, the experiments in Hardy et al. [31] were performed on human specimens from the older population. Comparisons of material properties of porcine brain tissue for different ages groups have been reported [29][33], where older age groups presents stiffer materials responses.

The re-optimization of the brain material parameters from Rycman et al. [27]) that was performed in this study was prompted by observed deviations in the verification results (see section 4.3.2). The verification simulations were based on simplified single element models, whereas Rycman et al. [27] used multi-element models. In multi-element configurations, lateral expansion (bulging) of the specimen geometry is possible, which could explain the observed differences.

5.2.1 Conclusion on the Brain Material

The validation results indicate that the Ogden rubber material model is relatively good at representing different types of brain tissue and its material behavior. To achieve optimal biofidelity for the head and brain models however, good material representation is not sufficient and factors such as geometry, meshing and contacts need to be properly considered.

5.3 Limitations

Regarding the verification and validation of the skull's response with MAT_187, several limitations must be acknowledged. First, the number of experimental tests available for the validations was relatively small and all the PMHS heads that were tested were smaller than the baseline VIVA+ head model. To compensate for this size discrepancy, a uniform, isotropic scale was applied. However, this scaling method is not entirely precise. Instead of applying a uniform scale to the entire head model, the scaling process should ideally aim to explicitly adjust specific anatomical features, such as scalp and skull thickness, to better reflect the exact dimensions of the physical test specimens.

Furthermore, due to scarcity of relevant material data, this study focused exclusively on the cortical bone. The trabecular bone layer was therefore not investigated, meaning its specific contribution to the overall structural response of the skull is a limitation that remains to be addressed in future work. Finally, regarding the material characterization of the cortical bone, the shear stiffness was not derived from direct shear testing. Instead, it was fully inferred from the available tensile test data. Since bone exhibits complex, multi-axial stress responses, relying solely on tensile data to define the shear behavior is a simplification that may limit the model's accuracy.

Another technical limitation was encountered regarding the software solver. The solver version used for these simulations (version 12.2 in LS-Dyna) was unable to precess the input for Young's modulus as a function of strain rate using a natural logarithmic scale. Utilizing a newer solver (such as 16.1) capable of interpreting logarithmic scale inputs for this material curve could potentially enhance the accuracy of the material representation and yield slightly more reliable results.

For the work related to the brain, the main limitation was the lack of scaling for the validation simulations. All validation simulations were performed using the same head model and without scaling. The head model closest in size to the average size of the experimental specimen in Hardy et al. was used [31]. Consequently, the positioning of the NDT models differs in varying degrees from the actual positions in the test subjects. This, in turn, likely results in different levels of relative displacements than would otherwise be expected.

Another limitation of the current study is that the VIVA+ head model lacks a detailed mesh representation of the meninges and dural reflections. Because these structures mechanically tether the brain and constrain its overall kinematic response, explicitly modeling them would likely reduce internal displacements, thereby improving the model's correlation with experimental impact data.

5.4 Future Work on the Skull and Brain Models

As observed during the verification process, the relationship defining the skull's yield stress as a function of plastic strain would benefit from further finetuning. This is particularly relevant for the female material model, which exhibited a more pronounced deviation from the regression curves at higher strain rates.

Additionally, since the drop test validations against Loyd et al. [23] solely utilized male specimens, future work should prioritize identifying and replicating validation cases specifically targeting female physical data to validate the female head model with implementation of MAT_187 for the skull. Finally, to improve the accuracy of subject specific simulations, future studies should explore more precise geometry scaling methods.

The VIVA+ model lacks integral parts of the brain in its mesh that could be leading to large displacements in the validation. It is not possible to conclude that the material parameters result in a sufficient representation of the brain while the model lacks these structures. Therefore, it is recommended to add these structures to the VIVA+ model before running new validation simulations.

Another recommendation is to add new validation cases. Hardy et al. report intracranial pressures during impacts that could be used for future validations [31]. Other studies such as the one by Alshareef et al. provide new load cases that can be replicated for validations [34].

The hyperelastic parameters were re-optimized to stresses in compression and tension and the implemented material model does not fit as well to shear stress. The viscoelastic parameters could also be re-optimized and for data that includes shear loading. This would improve the implemented material models behavior for shear conditions. It is possible that these improvements will not be too significant and the effects on the behavior of the other loading modes will need to be considered as not to cause unwanted compromises.

5.5 Data Availability

To ensure the reproducibility of this study, all files used in LS-Dyna simulations for this project are archived in a private Git repository hosted by Chalmers University of Technology. Because it is a private repository, public access i restricted. However, researchers interested in viewing or utilizing the files can access by contacting the project supervisors. The repository can be found at the following link: https://git.chalmers.se/me/vehicle-safety/bachelors-thesis/2026-bachelors-thesis-head/

Bibliography

[1] Johns Hopkins Medicine, “Head injury,” 2025. Accessed: 2026-02-10.

[2] “Skull fracture,” 2026. Encyclopedic overview of skull fractures.

[3] M. Majdan, D. Plancikova, A. Brazinova, M. Rusnak, D. Nieboer, V. Feigin, and A. Maas, “Epidemiology of traumatic brain injuries in europe: A cross-sectional analysis,” *The Lancet Public Health*, vol. 1, no. 2, pp. E76–E83, 2016.

[4] G. Smith, S. Hurite, and A. Yanik, “Human volunteer testing of gm air cushions,” in *Proceedings of National Automobile Engineering Meeting*, p. 11, 1972.

[5] N. Yoganandan, M. W. Arun, and F. A.Pintar, “Normalizing and scaling of data to derive human response corridors from impact tests,” *Journal of Biomechanics*, vol. 47, pp. 1749–1756, 2014.

[6] V. Team, “About viva+,” 2025. accessed 2026-04-29.

[7] J. John, C. klug, M. Kranjec, E. Svenning, and J. Iraeus, “Hello, world! viva+: A human body model lineup to evaluate sex-differences in crash protection,” *Journal of Front. Bioeng. Biotechnol.*, vol. 10, 2022.

[8] Livermore Software Technology Corporation, *LS-DYNA Keyword User’s Manual, Volume II*, 2023. Accessed: 2026-05-07.

[9] D. Dinkler and U. Kowalsky, *Introduction to Finite Element Methods.* Wiesbaden, Germany: Springer Vieweg, 2024.

[10] Ansys, Inc., *Ansys LS-DYNA User’s Guide, Release 2024 R2.* Ansys, Inc., Canonsburg, PA, 2024. Help System, Chapter 1: Introduction to LS-DYNA.

[11] Ansys, Inc., *ANSYS LS-DYNA Theory Manual.* Ansys, Inc., Canonsburg, PA, r16 ed., 2025. Revision R16@e545952c7, Released 03/21/2025.

[12] ANSYS, Inc., “What is explicit dynamics?.” `https://www.ansys.com/simulation-topics/what-is-explicit-dynamics`. Accessed May 8, 2026.

[13] J. L. Wood, “Mechanical properties of human cranial bone in tension,” 1969.

University Microfilms, A Xerox Company.

[14] J. L. Wood, “Dynamic response of human cranial bone,” *Journal of Biomechanics*, vol. 4, pp. 1–12, 1971.

[15] A. Back, S. Granholm, L. Larsson, and H. Viberg, “Age-dependent material modelling of the human cranium,” 2025.

[16] Johns Hopkins Medicine, “Anatomy of the brain.” `https://www.hopkinsmedicine.org/health/conditions-and-diseases/anatomy-of-the-brain`. Accessed: [07-05-2026].

[17] Encyclopædia Britannica, “Cerebellum, illustration.” Britannica ImageQuest. [Photograph]. Accessed: May 12, 2026.

[18] Encyclopædia Britannica, “Biomedical illustration of the meninges o..” Britannica ImageQuest. [Photograph]. Accessed: May 12, 2026.

[19] R. L. Drake, A. W. Vogl, and A. W. M. Mitchell, *Gray’s Anatomy for Students*. Philadelphia: Churchill Livingstone, 3rd ed., 2014.

[20] B. Rashid, M. Destrade, and M. D. Gilchrist, “Mechanical characterization of brain tissue in compression at dynamic strain rates,” *Journal of the Mechanical Behavior of Biomedical Materials*, vol. 10, pp. 23–38, 2012.

[21] S. Budday, R. Nay, R. de Rooij, P. Steinmann, T. Wyrobek, T. C. Ovaert, and E. Kuhl, “Mechanical properties of gray and white matter brain tissue by indentation,” *Journal of the Mechanical Behavior of Biomedical Materials*, vol. 46, pp. 318–330, 2015.

[22] D. Raymond, C. Van Ee, G. Crawford, and C. Bir, “Tolerance of the skull to blunt ballistic temporo-parietal impact,” *Journal of Biomechanics*, vol. 42, no. 15, pp. 2479–2485, 2009.

[23] A. M. Loyd, R. W. Nightingale, Y. Song, J. F. Luck, H. Cutcliffe, B. S. Myers, and C. D. Bass, “The response of the adult and atd heads to impacts onto a rigid surface,” *Accident Analysis and Prevention*, vol. 72, pp. 219–229, 2014.

[24] A. M. Loyd, *Studies of the Human Head from Neonate to Adult: An Inertial, Geometrical and Structural Analysis with Comparisons to the ATD Head*. Phd dissertation, Duke University, Durham, NC, 2011.

[25] “Head injury criterion,” 2024. Accessed: 2026-04-30.

[26] “Instrumentation for impact test—part 1: Electronic instrumentation,” Mar. 1995. Revised March 1995, originally issued 1970.

[27] A. Rycman, M. Bustamante, and D. Cronin, “Brain material properties and integration of arachnoid complex for biofidelic impact response for human head

finite element model," *Annals of Biomedical Engineering*, vol. 52, 01 2024.

[28] D. Lyu, R. Zhou, C.-h. Lin, P. Prasad, and L. Zhang, "Development and validation of a new anisotropic visco-hyperelastic human head finite element model capable of predicting multiple brain injuries," *Frontiers in Bioengineering and Biotechnology*, vol. Volume 10 - 2022, 2022.

[29] Z. Li, C. Ji, D. Li, R. Luo, G. Wang, and J. Jiang, "A comprehensive study on the mechanical properties of different regions of 8-week-old pediatric porcine brain under tension, shear, and compression at various strain rates," *Journal of Biomechanics*, vol. 98, p. 109380, 10 2020.

[30] Z. Li, H. Yang, G. Wang, X. Han, and S. Zhang, "Compressive properties and constitutive modeling of different regions of 8-week-old pediatric porcine brain under large strain and wide strain rates," *Journal of the Mechanical Behavior of Biomedical Materials*, vol. 89, pp. 122–131, 2019.

[31] W. N. Hardy, M. J. Mason, C. D. Foster, C. S. Shah, J. M. Kopacz, K. H. Yang, A. I. King, J. Bishop, M. Bey, W. Anderst, and S. Tashman, "A study of the response of the human cadaver head to impact," *Stapp Car Crash Journal*, vol. 51, pp. 17–80, 2007.

[32] M. Schachner, J. Micorek, P. Luttenberger, R. Greimel, C. Klug, and S. Rajinovic, "Dynasaur." Computer software.

[33] H. Fan, X. Jin, J. Hu, and K. Yang, "Age dependent material properties of infant and adolescent porcine brain," 08 2014. Proceedings of WSU 75th Anniversary Symposium Injury Biomechanics, Prevention, Diagnosis Treatment August 14-16, 2014, Detroit, MI, USA.

[34] A. Alshareef, J. S. Giudice, J. Forman, D. F. Shedd, K. A. Reynier, T. Wu, S. Sochor, M. R. Sochor, R. S. Salzar, and M. B. Panzer, "Biomechanics of the human brain during dynamic rotation of the head," *Journal of Neurotrauma*, vol. 37, pp. 1546–1555, jul 2020.

A

Loyd et al. Drop Test Velocities

Table A.1. Calculated initial impact velocities for specimen A01M.

Test ($\approx$ 15 cm Drops)	**Velocity** $[m/s]$	**Test ($\approx$ 30 cm Drops)**	**Velocity** $[m/s]$
Vertex	1.716	Vertex	2.426
Occiput	1.744	Occiput	2.418
Forehead	1.698	Forehead	2.426
Right Parietal	–	Right Parietal	2.410
Left Parietal	1.704	Left Parietal	2.446

Table A.2. Calculated initial impact velocities for specimen A02M.

Test ($\approx$ 15 cm Drops)	**Velocity** $[m/s]$	**Test ($\approx$ 30 cm Drops)**	**Velocity** $[m/s]$
Vertex	1.744	Vertex	2.426
Occiput	1.744	Occiput	2.418
Forehead	1.698	Forehead	2.426
Right Parietal	1.733	Right Parietal	2.410
Left Parietal	1.704	Left Parietal	2.446

Table A.3. Calculated initial impact velocities for specimen A04M.

Test ($\approx$ 15 cm Drops)	**Velocity** $[m/s]$	**Test ($\approx$ 30 cm Drops)**	**Velocity** $[m/s]$
Vertex	1.704	Vertex	2.410
Occiput	1.738	Occiput	2.410
Forehead	1.698	Forehead	2.438
Right Parietal	1.733	Right Parietal	2.438
Left Parietal	1.738	Left Parietal	2.414

Table A.4. Calculated initial impact velocities for specimen A05M.

Test ($\approx$ 15 cm Drops)	**Velocity** $[m/s]$	**Test ($\approx$ 30 cm Drops)**	**Velocity** $[m/s]$
Vertex	1.733	Vertex	2.426
Occiput	–	Occiput	–
Forehead	1.710	Forehead	2.438
Right Parietal	1.704	Right Parietal	2.438
Left Parietal	1.733	Left Parietal	2.414

Table A.5. Calculated initial impact velocities for specimen A06M.

Test ($\approx$ 15 cm Drops)	**Velocity** $[m/s]$	**Test ($\approx$ 30 cm Drops)**	**Velocity** $[m/s]$
Vertex	1.710	Vertex	2.426
Occiput	–	Occiput	–
Forehead	1.704	Forehead	2.422
Right Parietal	1.693	Right Parietal	2.434
Left Parietal	1.721	Left Parietal	2.410

Table A.6. Calculated initial impact velocities for specimen A07M.

Test ($\approx$ 15 cm Drops)	**Velocity** $[m/s]$	**Test ($\approx$ 30 cm Drops)**	**Velocity** $[m/s]$
Vertex	1.710	Vertex	2.422
Occiput	1.716	Occiput	2.434
Forehead	1.727	Forehead	2.410
Right Parietal	1.704	Right Parietal	2.422
Left Parietal	1.733	Left Parietal	2.426

B

Loyd et al. Drop Test Acceleration Results

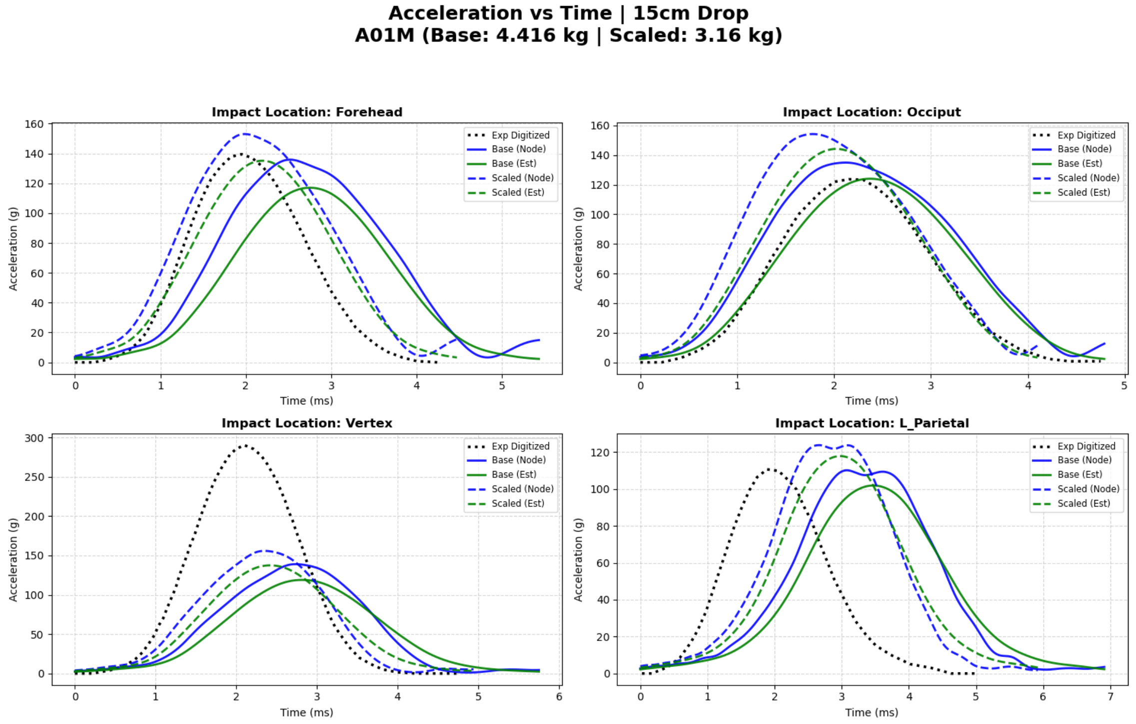

Figure B.1. Acceleration as a function of time for specimen A01M at drop height of 15 cm.

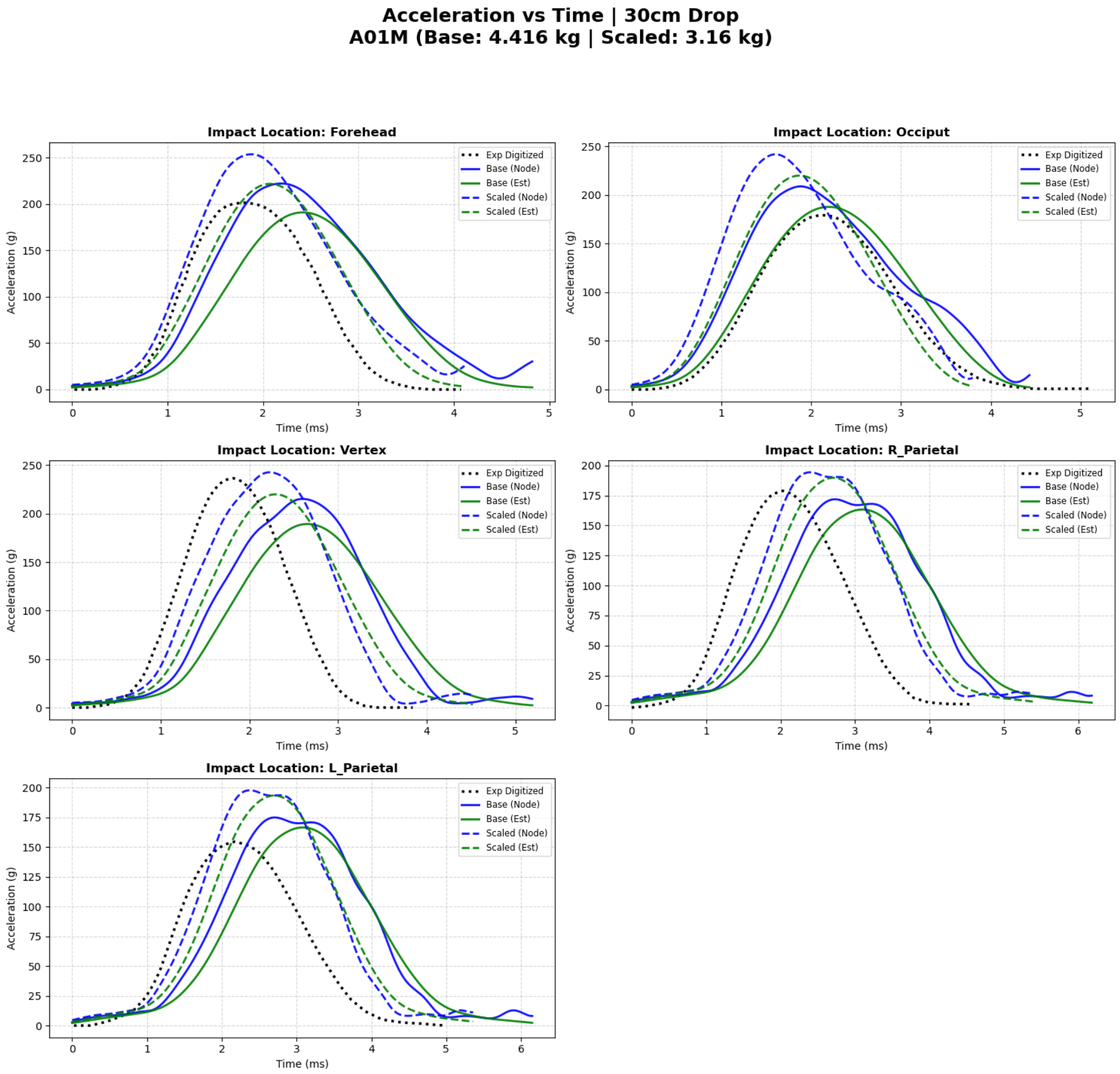

Figure B.2. Acceleration as a function of time for specimen A01M at drop height of 30 cm.

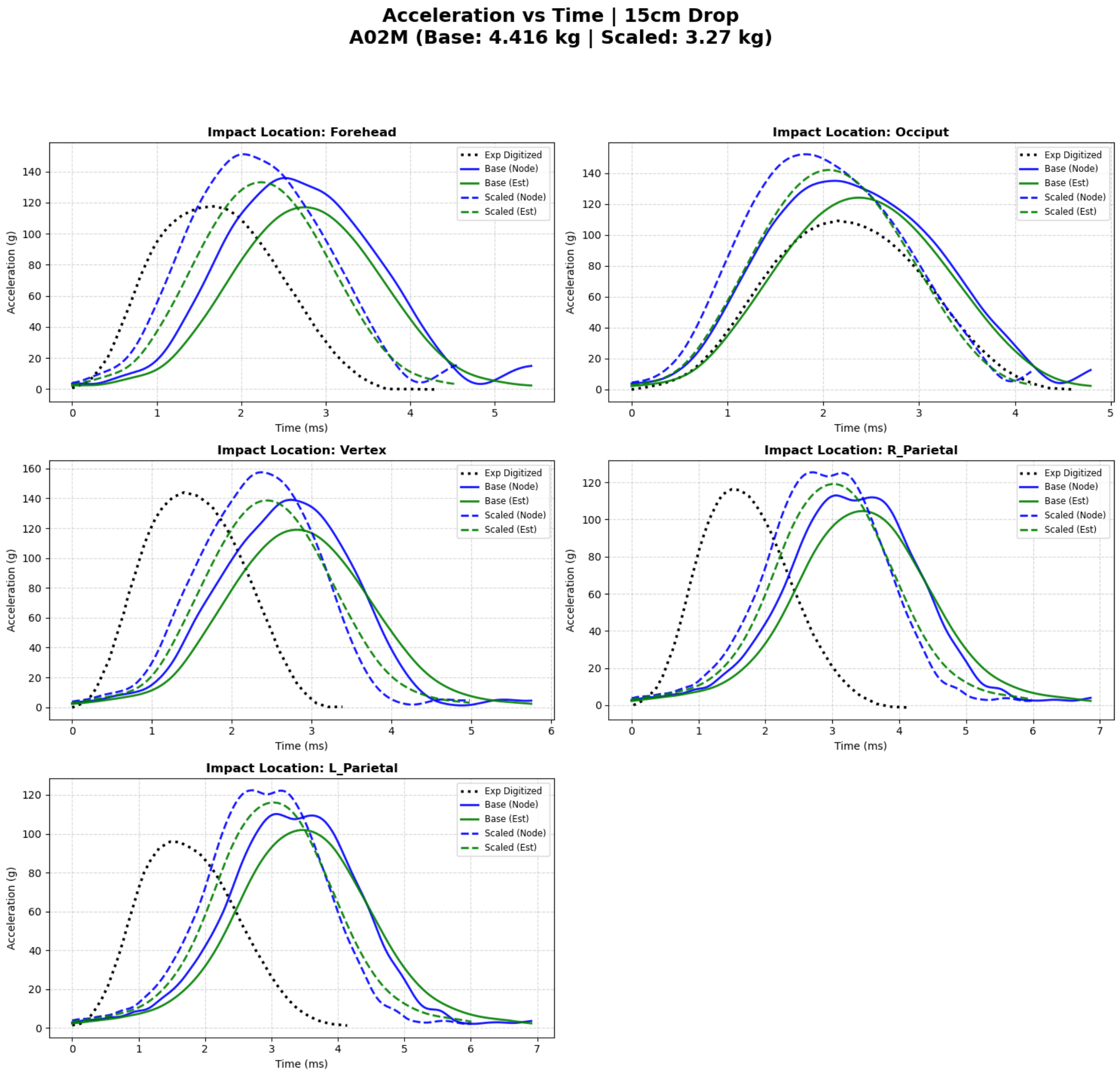

Figure B.3. Acceleration as a function of time for specimen A02M at drop height of 15 cm.

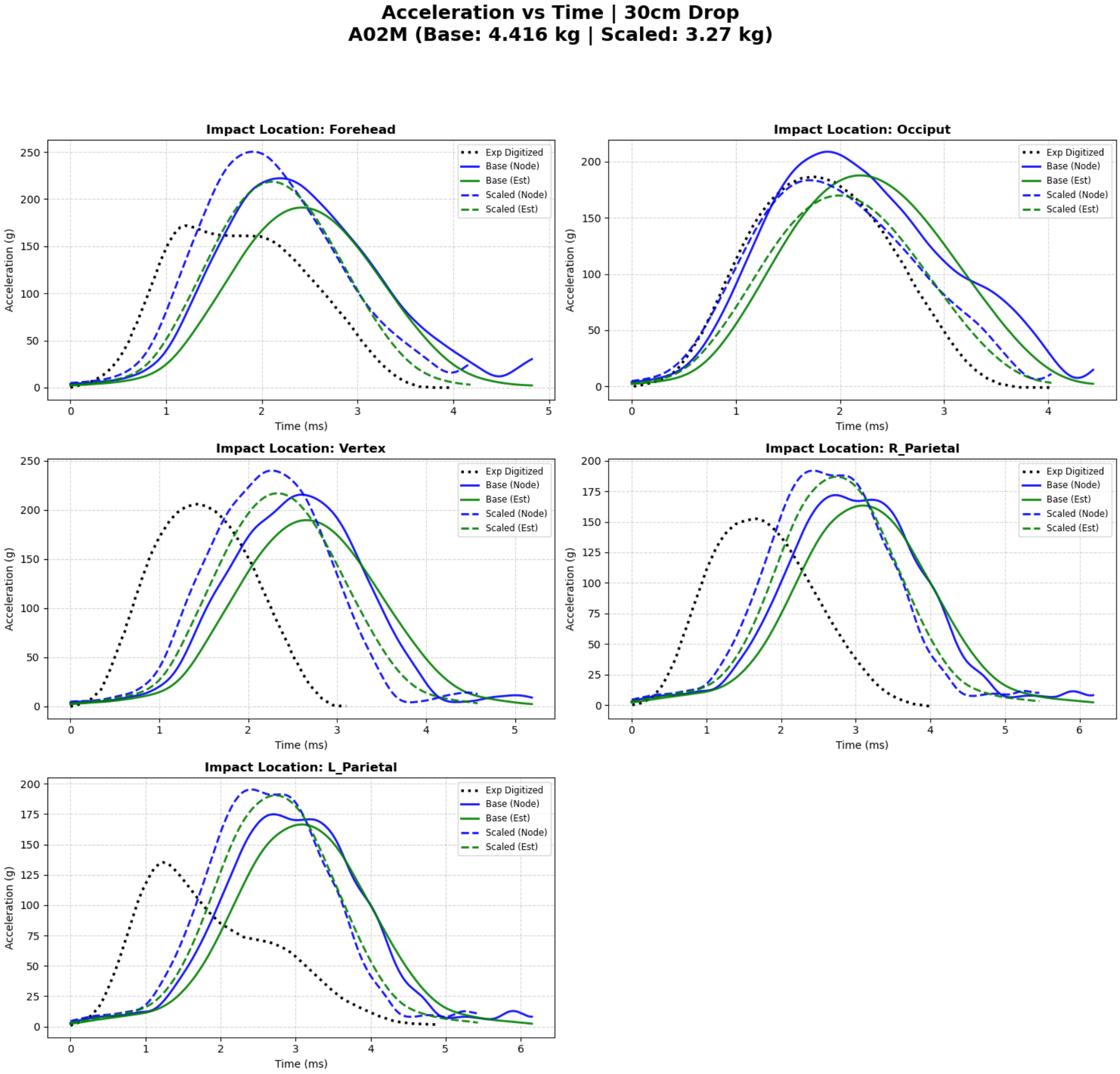

Figure B.4. Acceleration as a function of time for specimen A02M at drop height of 30 cm.

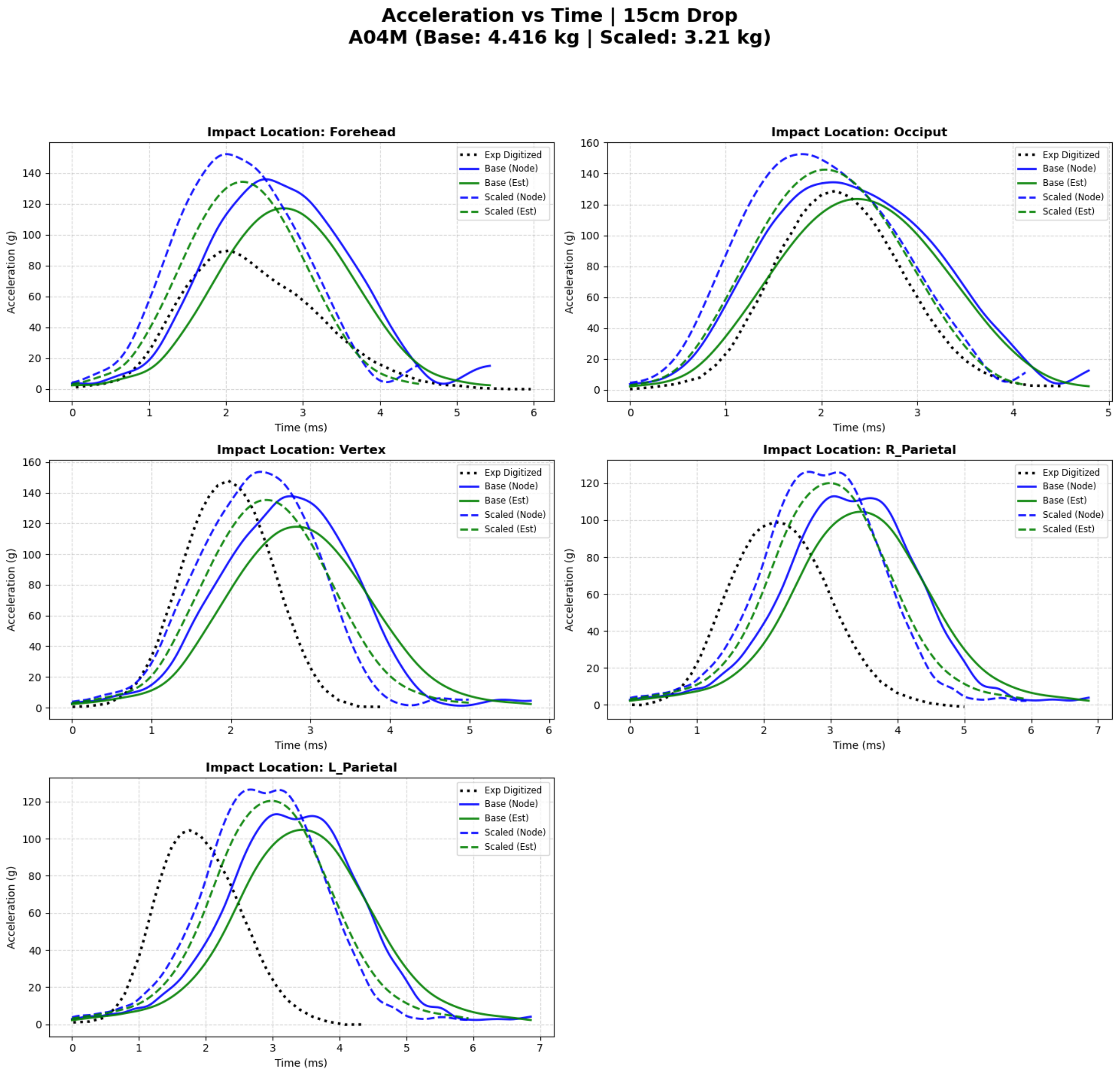

Figure B.5. Acceleration as a function of time for specimen A04M at drop height of 15 cm.

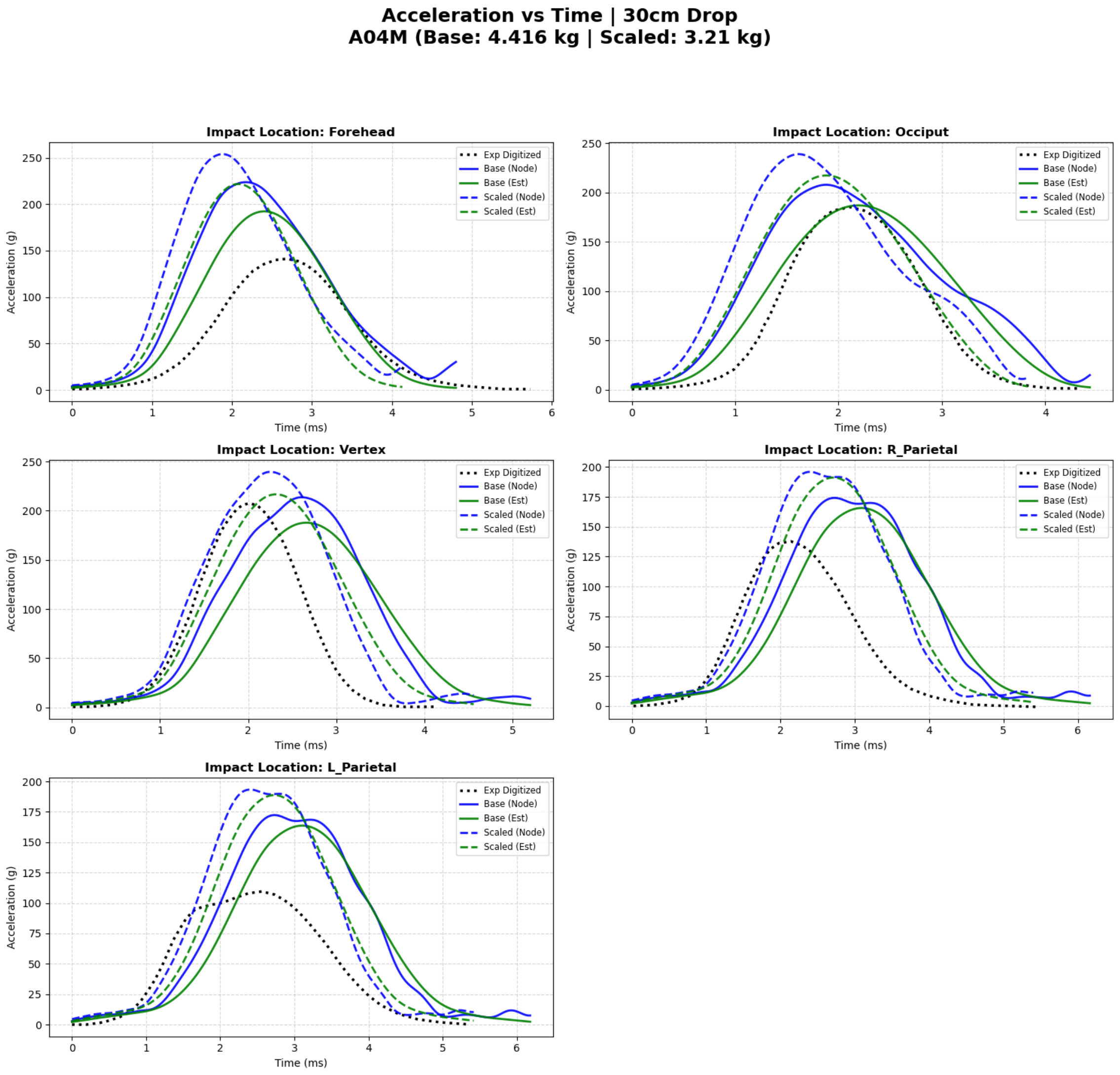

Figure B.6. Acceleration as a function of time for specimen A04M at drop height of 30 cm.

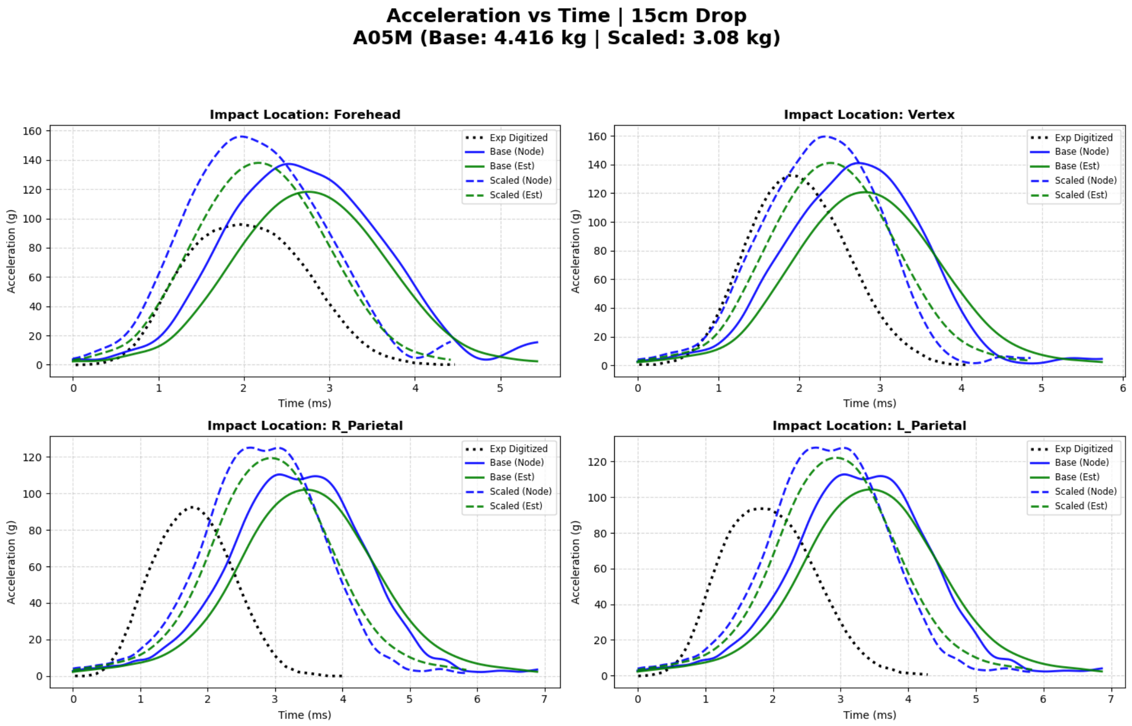

Figure B.7. Acceleration as a function of time for specimen A05M at drop height of 15 cm.

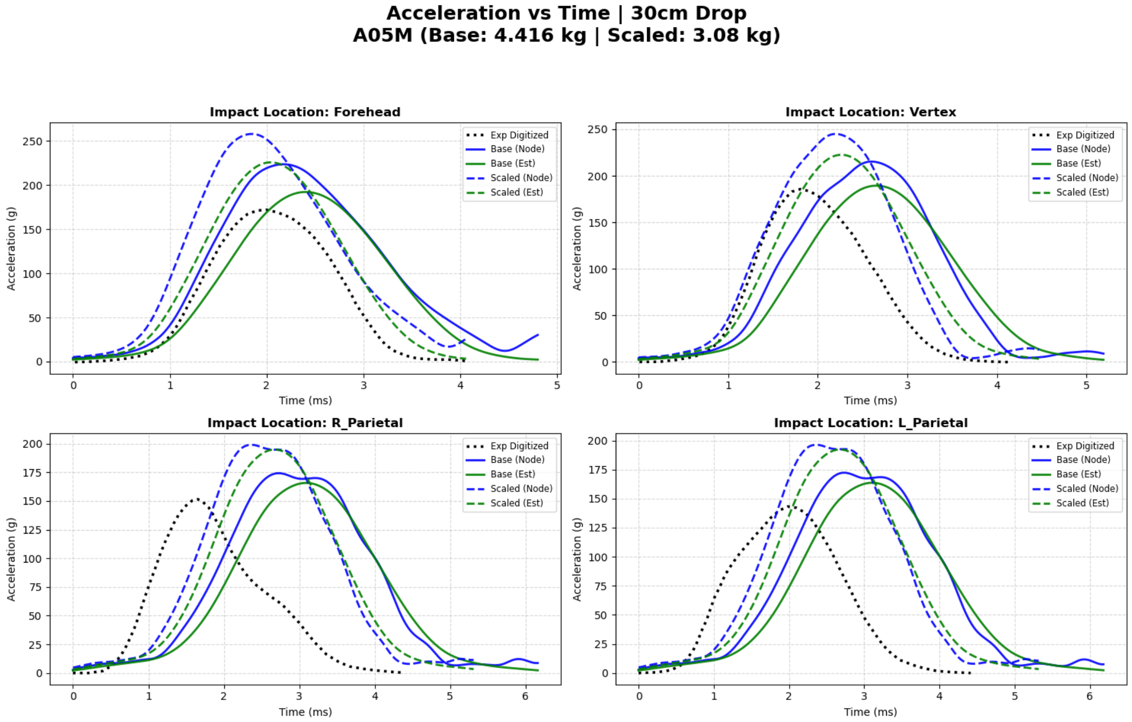

Figure B.8. Acceleration as a function of time for specimen A05M at drop height of 30 cm.

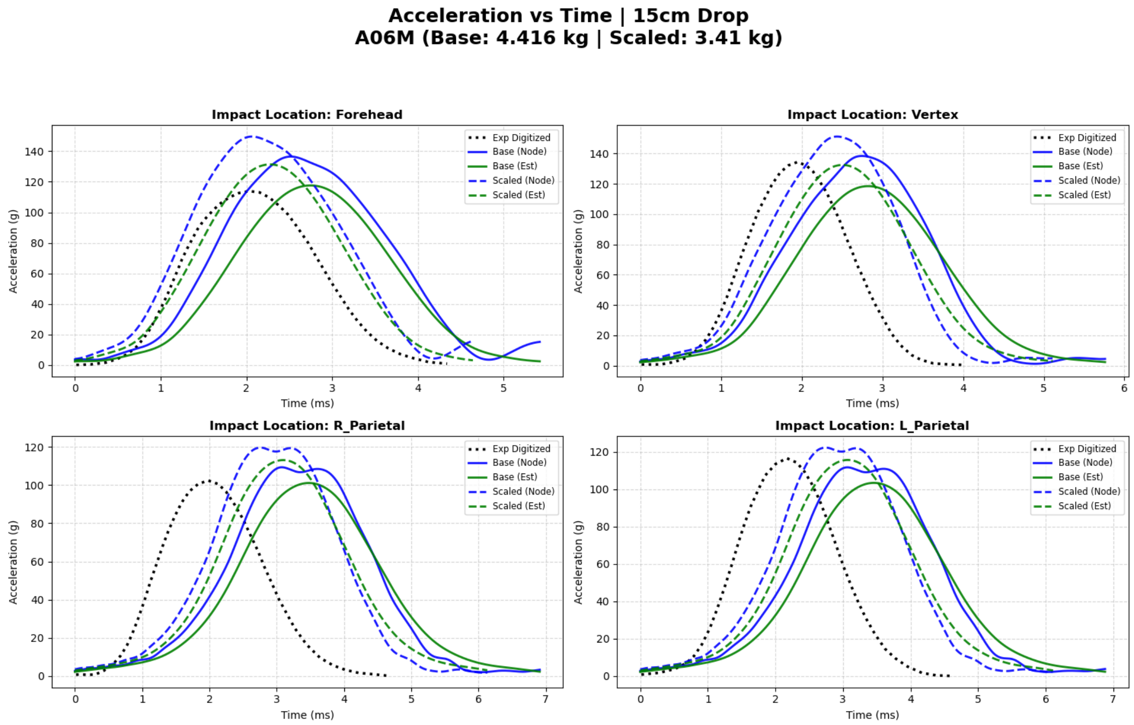

Figure B.9. Acceleration as a function of time for specimen A06M at drop height of 15 cm.

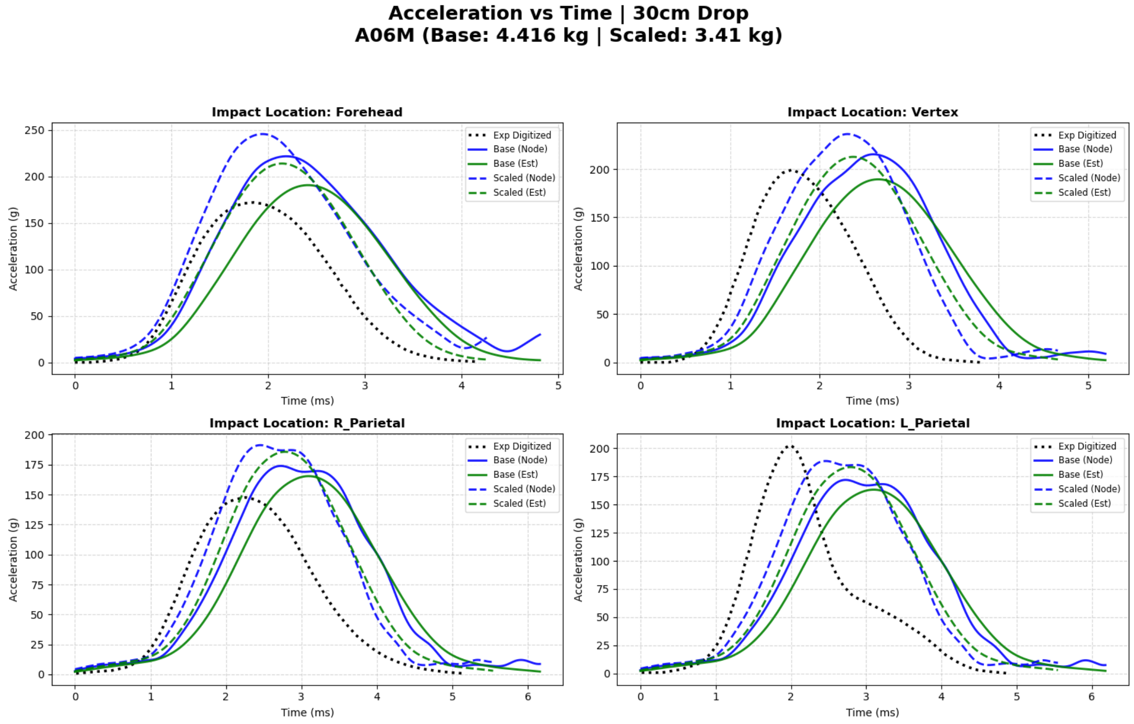

Figure B.10. Acceleration as a function of time for specimen A06M at drop height of 30 cm.

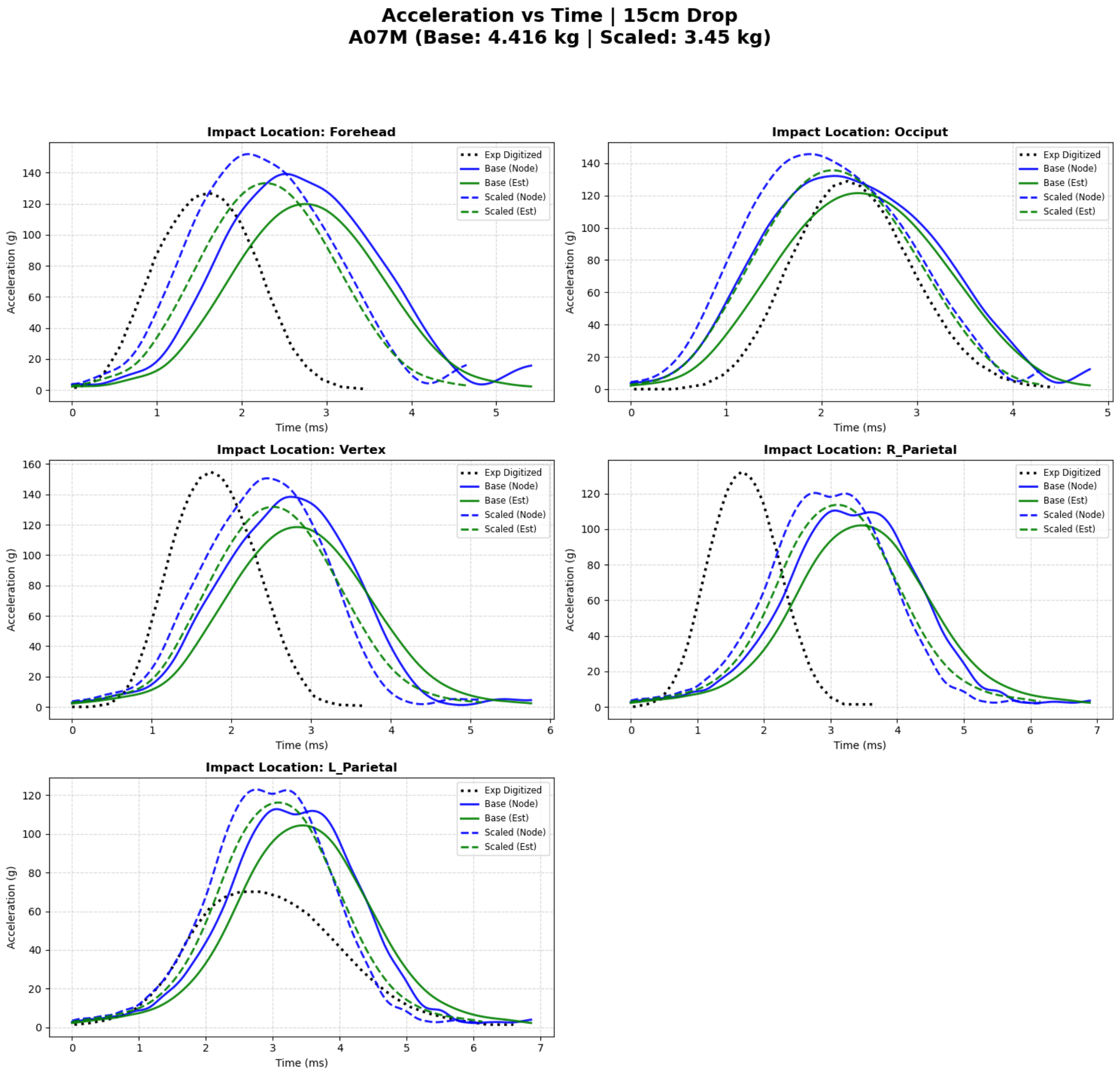

Figure B.11. Acceleration as a function of time for specimen A07M at drop height of 15 cm.

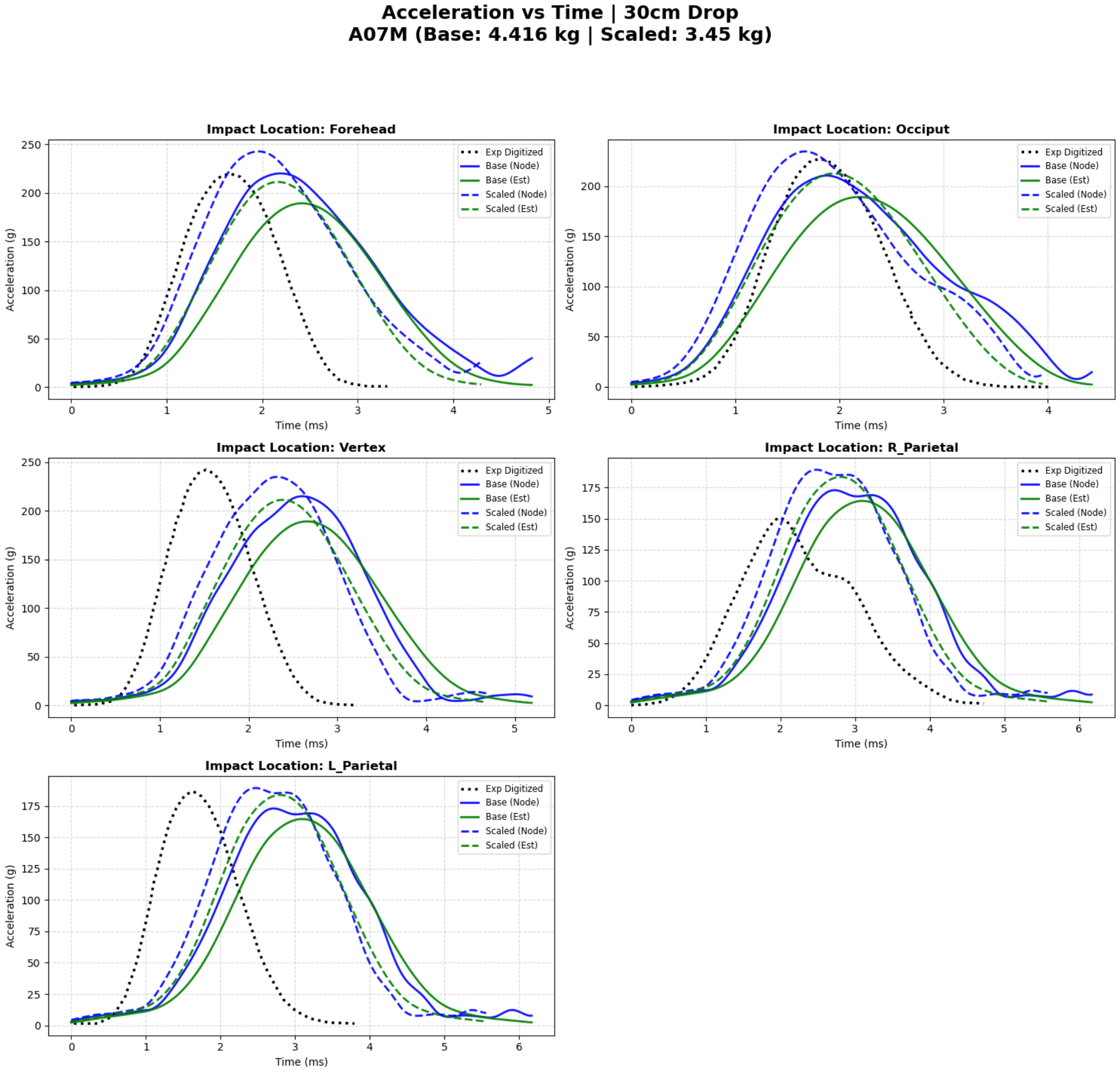

Figure B.12. Acceleration as a function of time for specimen A07M at drop height of 30 cm.

C

Rycman et al. Comparison of Verification Results

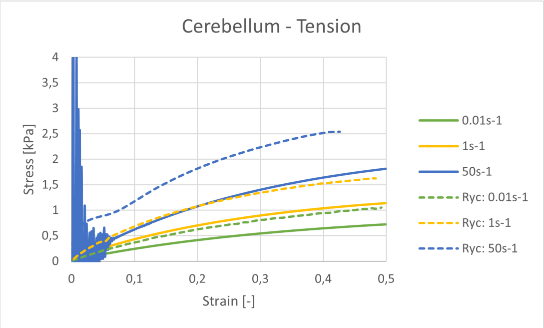

Figure C.1. Simualted material responses using baseline parameters vs correspinding responses reported in Rycman et al. [27] for cerebellum in tension.

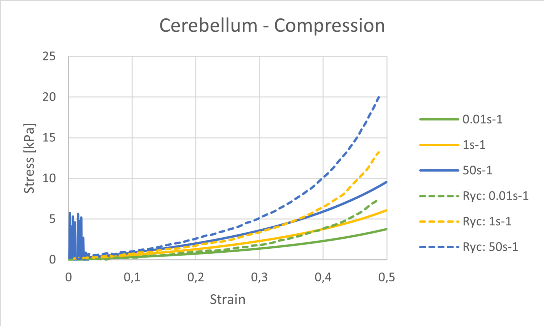

Figure C.2. Simualted material responses using baseline parameters vs correspinding responses reported in Rycman et al. [27] for cerebellum in compression.

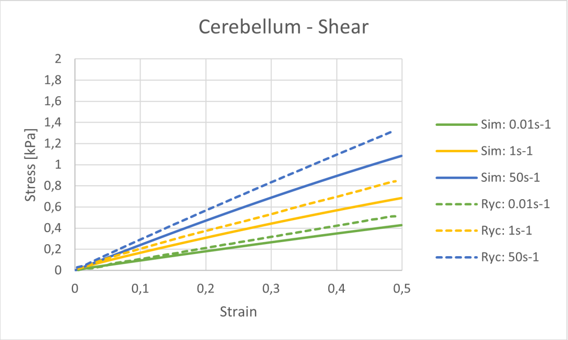

Figure C.3. Simualted material responses using baseline parameters vs correspinding responses reported in Rycman et al. [27] for cerebellum in shear.

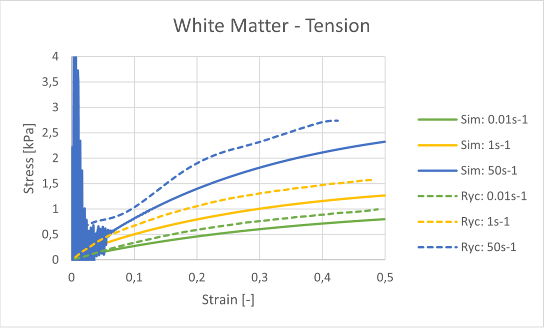

Figure C.4. Simualted material responses using baseline parameters vs correspinding responses reported in Rycman et al. [27] for white matter in tension.

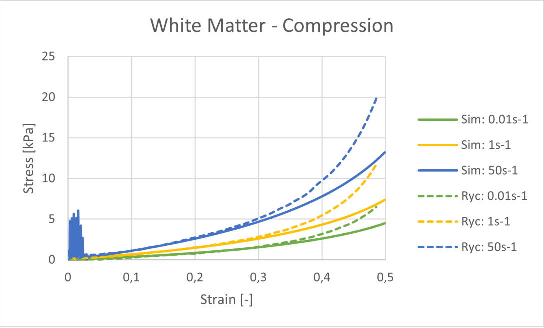

Figure C.5. Simualted material responses using baseline parameters vs correspinding responses reported in Rycman et al. [27] for white matter in compression.

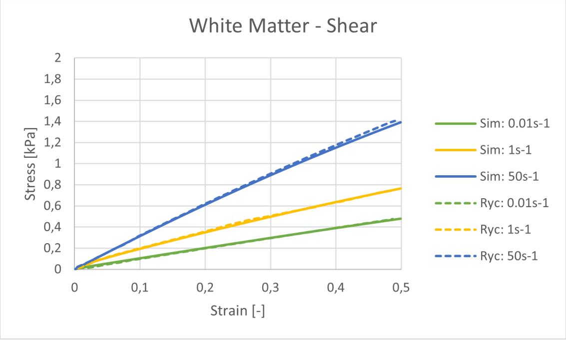

Figure C.6. Simualted material responses using baseline parameters vs correspinding responses reported in Rycman et al. [27] for in shear.white matter

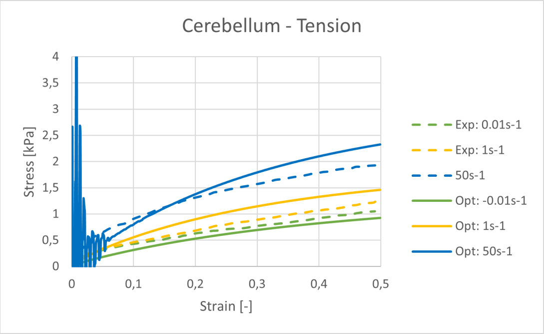

Figure C.7. Optimized material model response vs experimental response for cerebellum in tension.

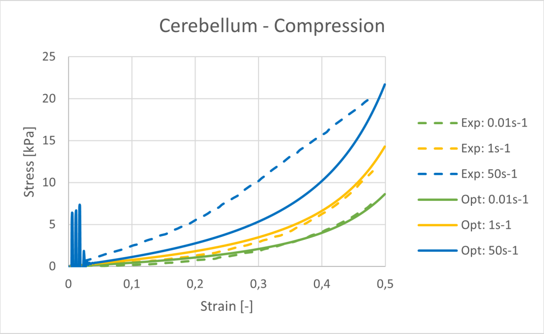

Figure C.8. Optimized material model response vs experimental response for cerebellum in compression.

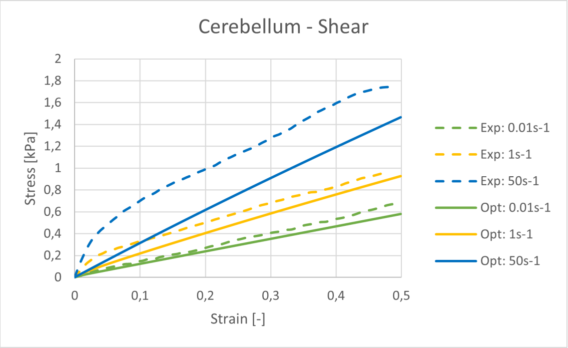

Figure C.9. Optimized material model response vs experimental response for cerebellum in shear.

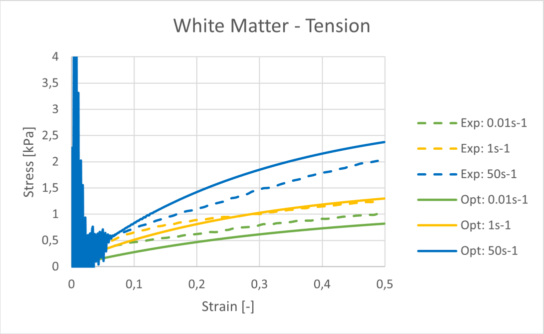

Figure C.10. Optimized material model response vs experimental response for white matter in tension.

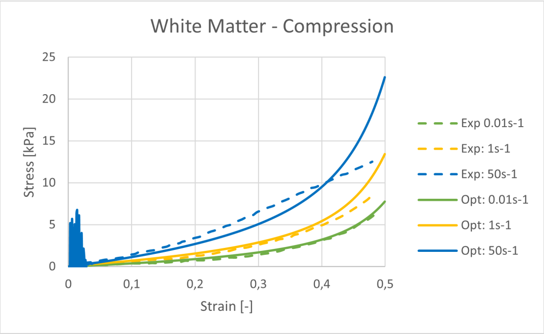

Figure C.11. Optimized material model response vs experimental response for white matter in compression.

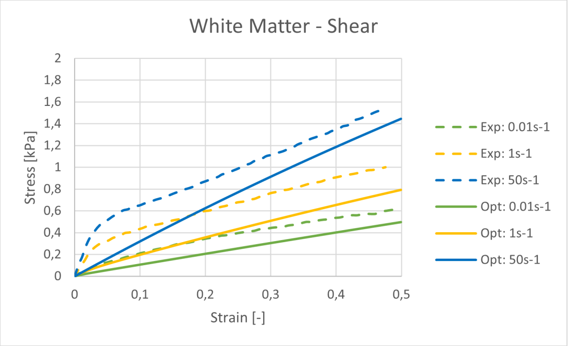

Figure C.12. Optimized material model response vs experimental response for white matter in shear.

D

Hardy et al. Relative Displacement Results

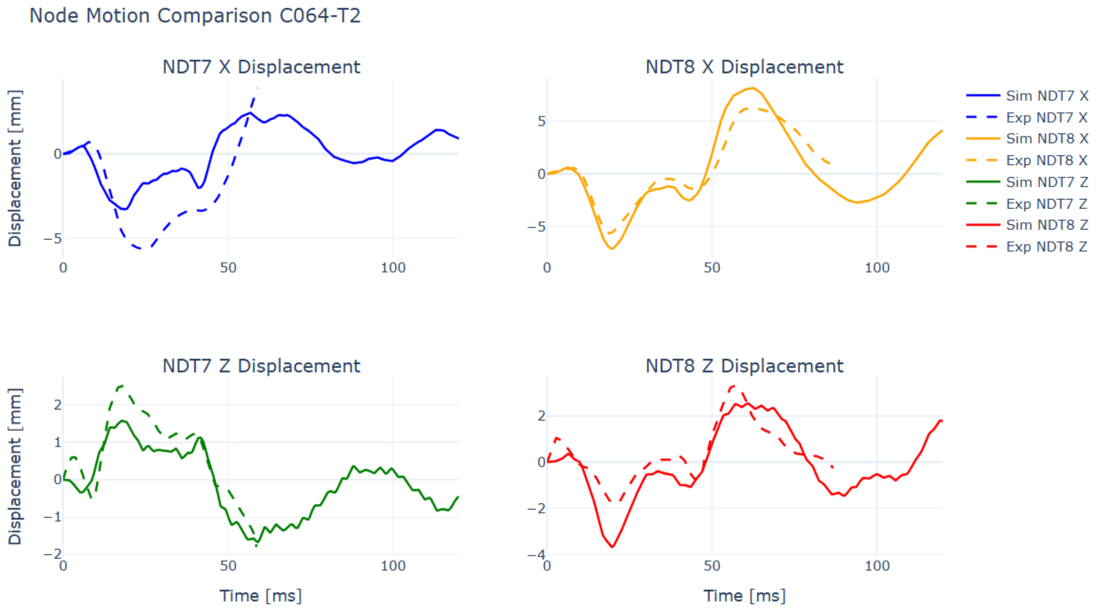

Figure D.1. Test C064-T2 with offset impact in median plane to the occipital region with helmet.

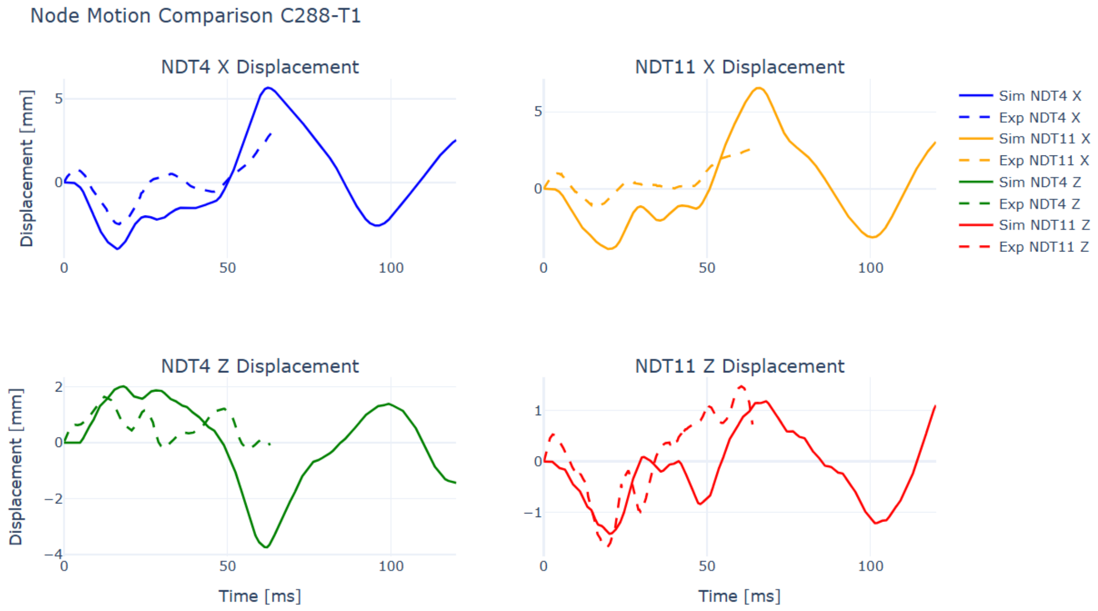

Figure D.2. Test C288-T1 with aligned impact in median plane to the occipital region with helmet.

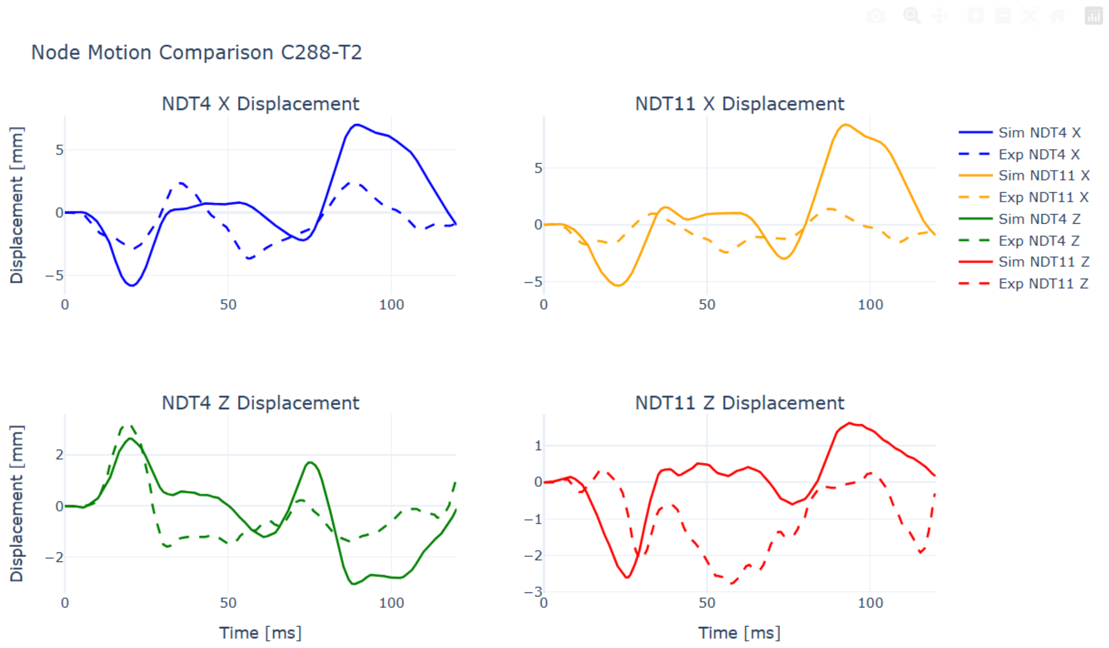

Figure D.3. Test C288-T2 with offset impact in median plane to the occipital region with helmet.

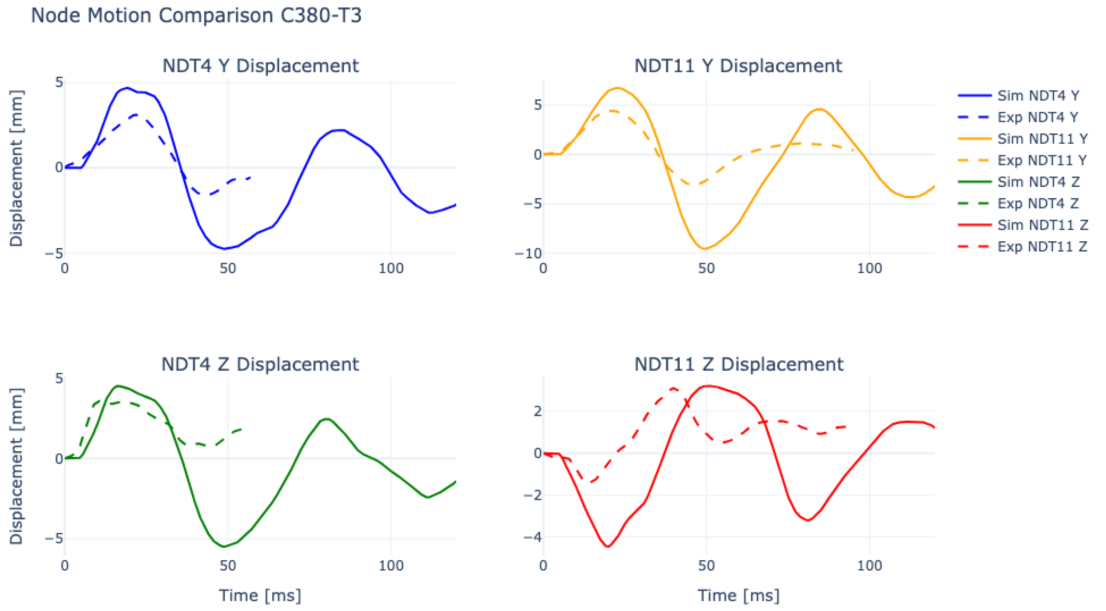

Figure D.4. Test C380-T3 with aligned impact in coronal plane to the temporal lt. region with helmet

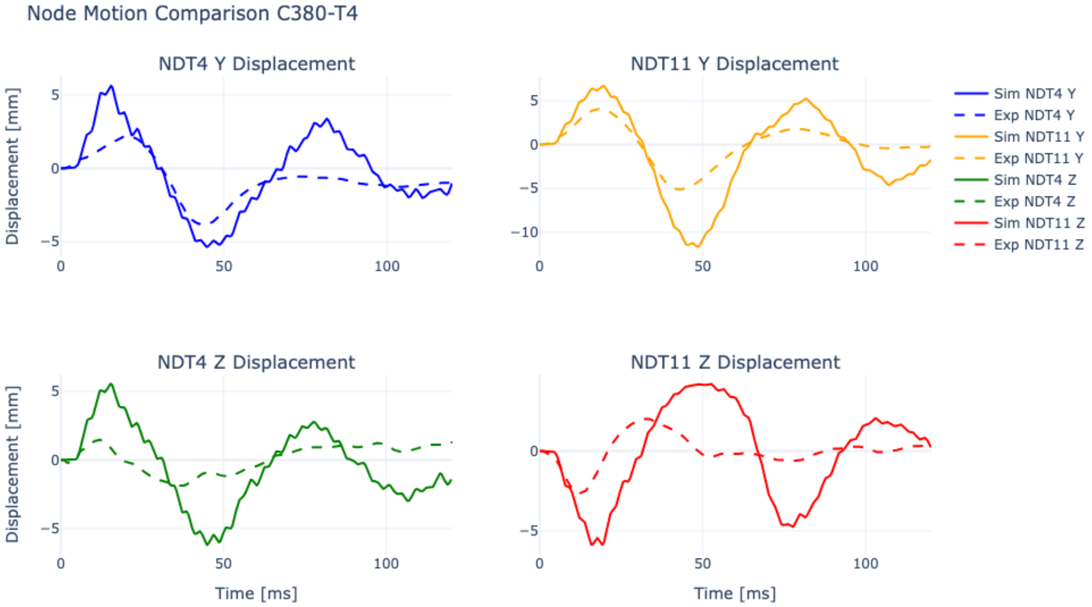

Figure D.5. Test C380-T4 with offset impact in coronal plane to the temporal lt. region without helmet.

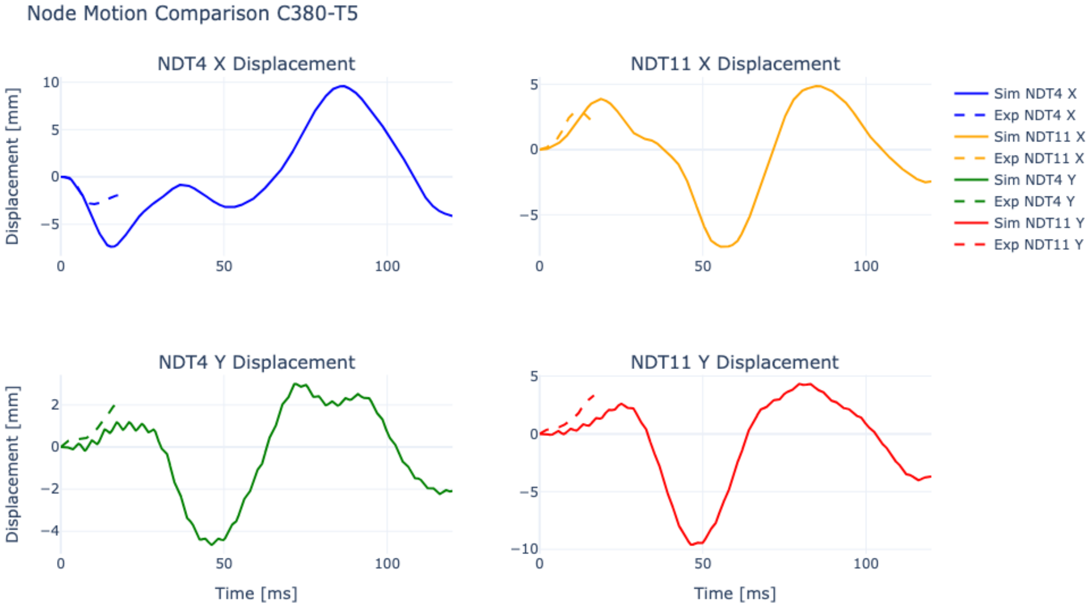

Figure D.6. Test C380-T5 with offset impact in horizontal plane to the parietal lt. region without helmet.

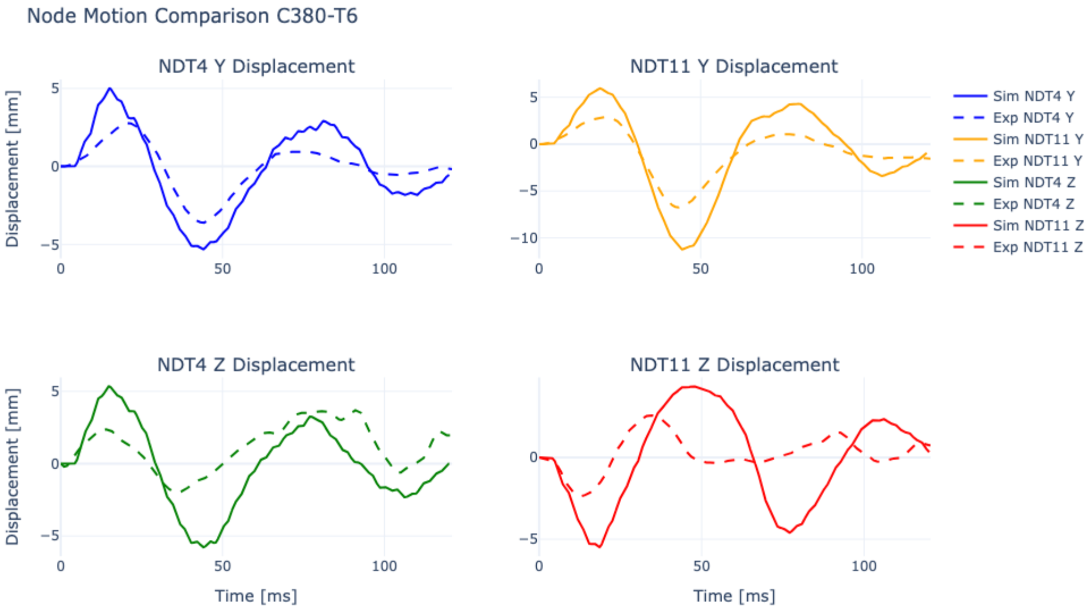

Figure D.7. Test C380-T6 with aligned impact in coronal plane to the temporal lt. region without helmet.

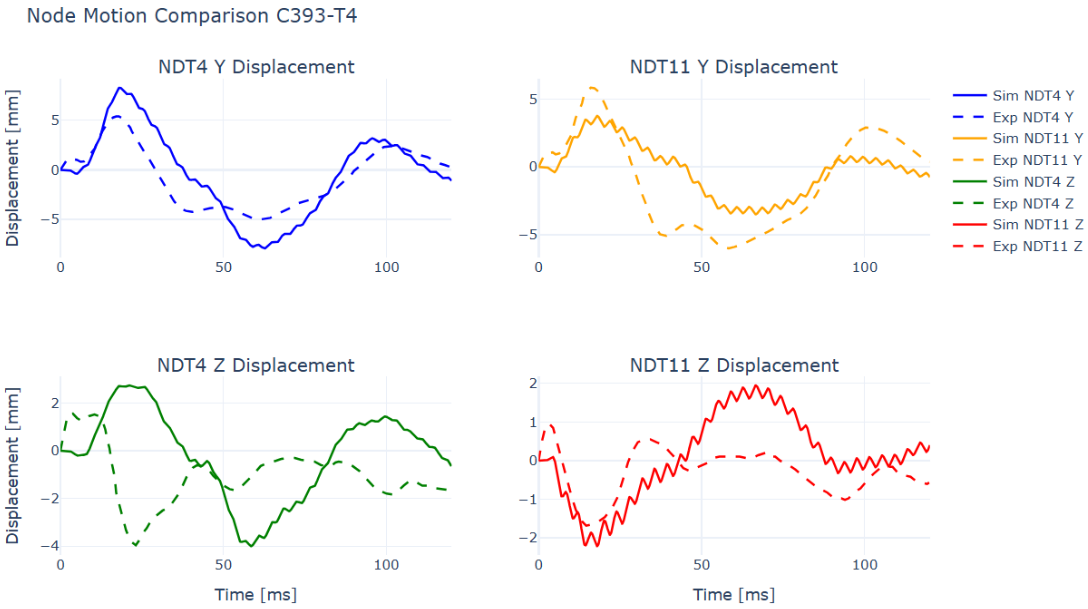

Figure D.8. Test C393-T4 with offset impact in coronal plane to the temporal lt. region without helmet.

E

Relative Displacement Results in Local and Global Coordinate Systems

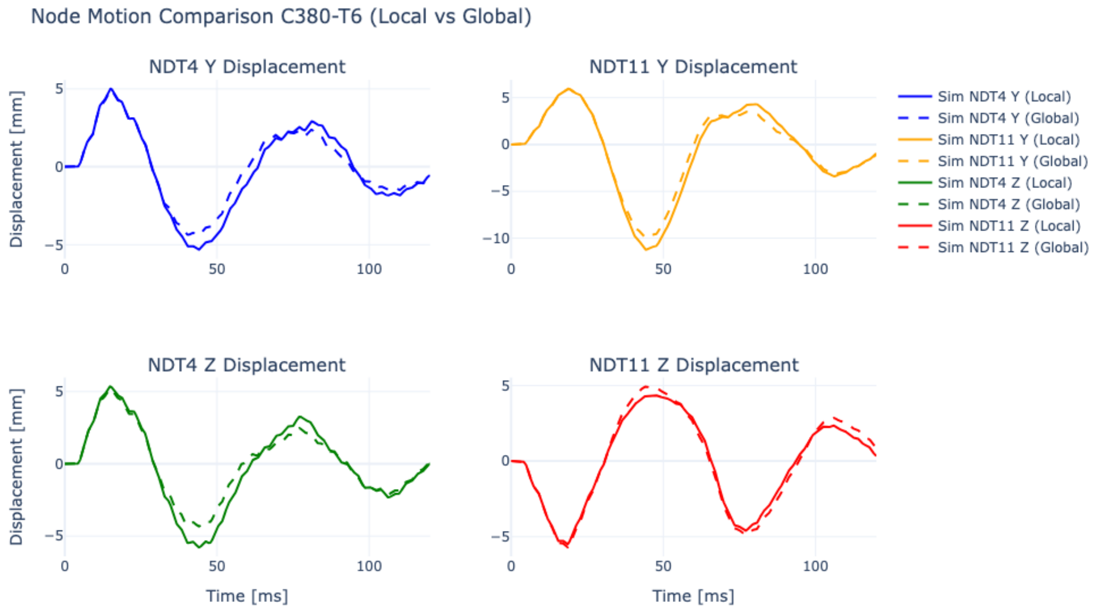

Figure E.1. Comparison between local coordinates (solid) and global coordinates (dashed) for C380-T6.

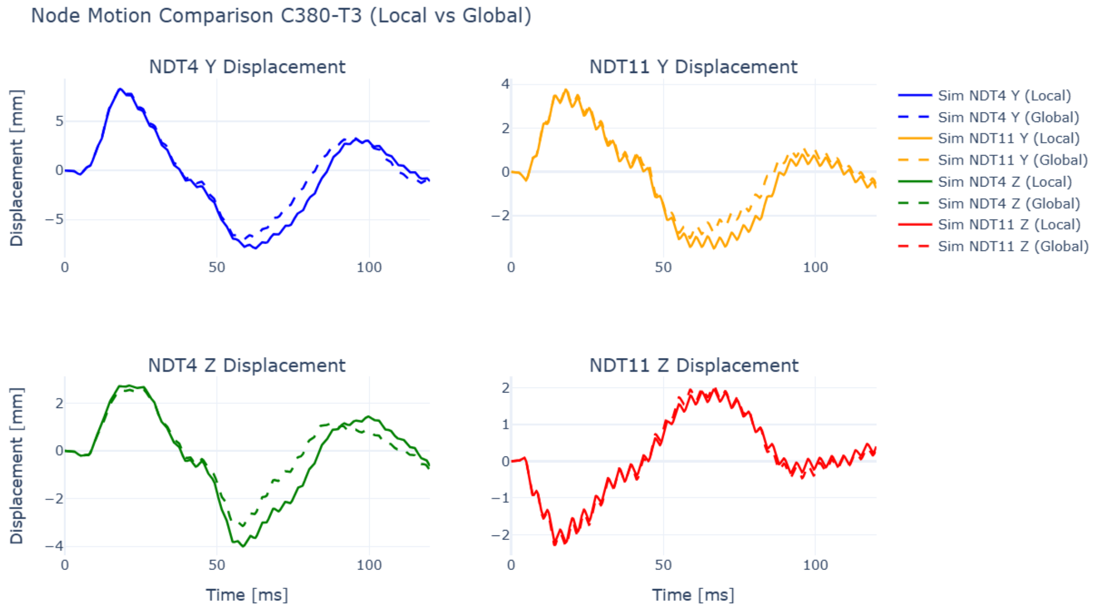

Figure E.2. Comparison between local coordinates (solid) and global coordinates (dashed) for C393-T4.

DEPARTMENT OF MECHANICS AND MARITIME SCIENCES
CHALMERS UNIVERSITY OF TECHNOLOGY
Gothenburg, Sweden 2026
www.chalmers.se

CHALMERS